Precambrian Plate Tectonics in Northern Hudson Bay: Evidence from P and S-wave Seismic Tomography and Analysis of Source Side Effects in Relative Arrival-Time Datasets.

Mitch.V. Liddell[1], Ian Bastow[1], Nicholas Rawlinson[2], Fiona Darbyshire[3], Amy Gilligan[4], and Emma Watson[1]

[1]Department of Earth Science and Engineering, Imperial College London, UK.
[2]University of Cambridge, UK.
[3]Université du Québec à Montréal, Canada.
[4]School of Geosciences, University of Aberdeen, UK.

Key Points:

- Evidence of Precambrian plate-scale underthrusting beneath Baffin Island
- Microplates within the Trans-Hudson Orogen are imaged, complicating the two-plate hypothesis; no seismic distinction at the STZ is observed
- Subducting slabs can contaminate relative arrival time residuals and frequency content. We analyze the effect and show it may be mitigated

Corresponding author: M.V. Liddell, m.liddell14@imperial.ac.uk

Abstract

The geology of northern Hudson Bay, Canada, documents more than 2 billion years of history including the assembly of Precambrian and Archean terranes during several Paleoproterozoic orogenies, culminating in the Trans-Hudson Orogen (THO) ~1.8 Ga. The THO has been hypothesized to be similar in scale and nature to the ongoing Himalaya-Karakoram-Tibetan orogen, but the nature of lithospheric terrane boundaries, including potential plate-scale underthrusting, are poorly understood. To address this problem we present new P and S-wave tomographic models of the mantle seismic structure using data from recent seismograph networks stretching from northern Ontario to Nunavut (60°W - 100°W and 50°N - 80°N). The large size of our network requires careful mitigation of the influence of source-side structure that contaminates our relative arrival time residuals. Our tomographic models reveal a complicated internal structure in the Archean Churchill plate. However, no seismic wavespeed distinction is observed across the Snowbird Tectonic Zone, which bisects the Churchill. The mantle lithosphere in the central region of Hudson Bay is distinct from the THO, indicating potential boundaries of micro-continents and lithospheric blocks between the principal colliders. Slow wavespeeds underlie southern Baffin Island, the leading edge of the generally high wavespeed Churchill plate. This is interpreted to be Paleoproterozoic material underthrust beneath Baffin Island in a modern-style subduction zone setting.

1 Overview

The northern Hudson Bay region in Canada comprises several major Archean (> 2.5 Ga) and Paleoproterozoic domains and collision zones. The region is underlain by a thick (> 250 km), high wavespeed lithospheric root [e.g., Darbyshire et al., 2013; Porritt et al., 2015] and contains the record of a ~1.8 Ga continental collision zone, the Trans-Hudson Orogen (THO) [e.g., Hoffman, 1988]. It is thus an ideal natural laboratory for the study of Precambrian tectonic processes.

Estimates for the onset of modern-style plate tectonics vary from the early Archean to the Proterozoic [e.g. Stern, 2005; Hopkins et al., 2008; Hawkesworth et al., 2017]. The early Earth was hotter and more ductile, which is thought to have hindered the onset of modern-style plate tectonics [e.g., Stevenson, 2003].However, the apparent stabilization of continental lithosphere and crust ~3 Ga, as well as the discovery of subduction-related eclogites of a similar age may point to an Archean emergence of plate tectonics [e.g., Hawkesworth et al., 2017, Tappe et al., 2011]. Regardless of when plate tectonics formally began, geological and geophysical consensus is emerging that the Proterozoic THO developed from modern-style plate tectonics [e.g., St-Onge et al., 2006; Thompson et al., 2010; Bastow et al., 2011; Weller and St-Onge, 2017]. Multiple theories exist regarding the details of THO development, ranging from a relatively simple two-plate orogeny [e.g., St-Onge et al., 2006, 2009] to more complex models including island arc and proto-continent accretion [e.g., Berman et al., 2005; Corrigan et al., 2009; Liddell et al., 2017]. Different THO assembly styles may change the way in which geophysical observations are interpreted, since plate tectonic processes can create large lateral offsets between the observed surface geology of the crust and mantle lithosphere. Resolving these issues requires an improved understanding of the deep seismic structure of the northern Hudson Bay region.Blocks of distinct composition, inherent since their formation, or as a result of metasomatism, would be expected to manifest as different mantle seismic wave speeds. Underthrust material could manifest as dipping structures or as an extension of wavespeed anomalies beneath the overriding region.

The structure of the mantle lithosphere in northern Hudson Bay has previously been constrained by global and regional surface wave models. The Canadian shield was once viewed as a homogeneous fast wavespeed block with no distinction between Archean and less-depleted Proterozoic mantle. [e.g., Shapiro and Ritzwoller, 2002; Darbyshire and

Eaton, 2010; Ritsema et al., 2011]. More recently, models have revealed the THO as a relatively slow band of lithosphere between the Churchill and Superior plates [Figure 1; eg., Darbyshire et al., 2013]. The detailed architecture of this band is unclear, however, due to the relatively poor lateral resolving power of surface waves.

To address outstanding questions about the THO and the internal architecture of the lithosphere beneath northern Hudson Bay, we provide the first dedicated P and S-wave tomographic study in the region. Our network comprises 64 seismograph stations distributed around Hudson Bay and the islands to the north (Figure 1). We take particular care to assess the validity of the relative arrival-time method for such a large network. Specifically, we test whether and to what degree the effect of source-side structure is removed during the calculation of our relative arrival time residuals.

2 Tectonic Background

The northern Hudson Bay region is dominated by the Superior and Churchill cratons [Figure 1; Hoffman, 1988]. The Churchill is divided into the Rae and the Hearne along the Snowbird Tectonic Zone (STZ). The subdivisions are distinguished geologically by a lack of post 2.66 Ga magmatism in the Hearne [e.g. Davis et al., 2006]. Several potential origins of the STZ have been proposed, and the east and west regions may even have different lithospheric structure [Bao and Eaton, 2015]. In our study region, the STZ is exposed on the western coast of Hudson Bay and potentially extends to Southampton Island [Spratt et al., 2012]. It is characterized by high pressure metamorphic belts, pointing to a ~1.9 Ga collision [e.g., Berman et al., 2007]. The central Rae craton includes several distinct blocks, suggesting it may also have a complex internal tectonic history [e.g., Skulski et al., 2003].

The THO marks the ~1.8 Ga collision of Archean domains with the Superior acting as a double indenter into the Churchill [Gibb, 1983; Darbyshire and Eaton, 2010]. Other studies have used the term THO more broadly to define the entire region of structural and metamorphic overprint due to the collision [e.g., Corrigan et al., 2009]. Under this definition the internides of the collision zone itself are defined as the 'Reindeer Zone'. The physical extent of this broader definition includes most of our study region and the entire region of resolution in our inversion models, thus rendering it less useful for our purposes. We therefore use 'THO' in this study to refer to the remains of the collision zone itself and not the wider region of deformation. It is the largest orogen that contributed to the creation of the Paleoproterozoic supercontinent Columbia [Rogers and Santosh, 2002], and is broadly understood to have formed by the closure of the Manikewan Ocean [e.g., Hoffman, 1988; St-Onge et al., 2006, 2009]. The THO stretches >4600 km from central North America to Greenland and is on average ~500 km wide [St-Onge et al., 2006], although widths of 700 km have been suggested in northern Hudson Bay and Baffin Island [Gilligan et al., 2016; Liddell et al., 2017]. The THO developed from a series of smaller orogenies [see Corrigan et al., 2009, and references therein]. The first of these is the 1.92-1.89 Ga Snowbird Orogeny, with contemporaneous subduction beneath the western Superior craton; the modern STZ is what remains of this orogeny [e.g., Berman et al., 2007]. This was followed by addition of the Meta-Incognita micro-continent and the Sugluk block to the eastern Rae craton [Corrigan et al., 2009]. Terminal collision between the Churchill and Superior plate occurred from 1.83 to 1.80 Ga. This was synchronous with significant tectonothermal reworking, much of which occurred on the weaker, hotter, Churchill province [St-Onge et al., 2006]. The THO may have involved a number of smaller microcontinents that were swept up between the larger blocks during ocean closure [e.g., Corrigan et al., 2009]. Southern Baffin Island and north-central Hudson Bay has been postulated to be an amalgamation of some of these micro-continents [St-Onge et al., 2006; Snyder et al., 2013]. Recently, high-pressure, low-temperature, eclogite rocks from within the THO have been found by Weller and St-Onge [2017]. These are thought to fill a missing link in the geological record in this region, and provide compelling evidence for the operation of modern-style plate tectonics by 1.8 Ga.

3 Previous Geophysical Studies

P and S-wave global tomographic models reveal fast wavespeeds beneath most of North America east of the Rocky Mountains to ≥250 km depth [e.g., Li et al., 2008; Lebedev and Van Der Hilst, 2008; Ritsema et al., 2011; Schaeffer and Lebedev, 2013], but these fast wavespeeds are not thought to have resulted in any thermally-driven topography on the mantle transition zone [Thompson et al., 2011]. The seismic structure of the upper mantle of the western Superior province was constrained with P and S-wave models by Sol et al. [2002]. The authors found evidence for a ~300 km thick cratonic root, and interpreted a deep high-velocity anomaly as a remnant Archean-age subducted slab. Further work on the Superior province by Frederiksen et al. [2007, 2013] found a significant

change in lithospheric mantle character between the west and east Superior, and imaged the mantle expression of the Superior/Trans-Hudson contact. These were both significant mantle velocity signatures that were unconnected to crustal expressions. Continent-wide receiver function results [e.g., Abt et al., 2010], and long-period waveform inversion [e.g., Yuan and Romanowicz, 2010; Yuan et al., 2011], have contributed to a picture of a continent-scale two-layer lithospheric model. North America is thought to have grown episodically, with a chemically depleted upper ~150-200 km underlain by younger, less depleted material. This change may be distinguished by a change in anisotropic fast direction [e.g., Darbyshire et al., 2013; Liddell et al., 2017; Petrescu et al., 2017]. Sharp discontinuities imaged at mid-lithospheric depths by receiver function studies throughout cratonic North America [Abt et al., 2010] and within northern Hudson Bay have supported this episodic growth theory [e.g. Rychert and Shearer, 2009; Porritt et al., 2015].

The UK Hudson Bay Lithospheric Experiment [HuBLE; e.g., Bastow et al., 2015] involved seismometers installed on the northern islands of the Hudson Strait and Baffin Island, complementing the existing POLARIS network [Eaton et al., 2005], and increasing the resolution in the northern part of the Bay dramatically. These, in combination with other seismograph networks, have been used to provide improved insight into the crustal structure [e.g., Thompson et al., 2010; Pawlak et al., 2011, 2012; Thompson et al., 2015; Gilligan et al., 2016], mantle wavespeed [e.g., Darbyshire et al., 2013], and mantle anisotropy [e.g., Bastow et al., 2011; Snyder et al., 2013; Liddell et al., 2017]. Based on two-station path-averaged Rayleigh wave dispersion analysis, Darbyshire and Eaton [2010] found no seismic wavespeed distinction between Archean and Proterozoic mantle. However, anisotropic surface wave tomographic models from Darbyshire et al. [2013] resolved slower Proterozoic material associated with the THO between the faster Archean Superior and Churchill cratons; they also estimated a Lithosphere-Asthenosphere Boundary (LAB) depth of ~250 km beneath the Bay and surrounding areas using a 1.7% fast shear velocity contour as a LAB proxy. Receiver function results from Porritt et al. [2015] showed an exceptionally thick lithosphere (~350 km) beneath central Hudson Bay and widespread mid-lithospheric discontinuities.

SKS splitting results by Bastow et al. [2011] showed that anisotropic fast directions were, to first order, controlled by the nearby THO, and variable anisotropic splitting parameters on Baffin Island were interpreted as being due to a potential dipping layer. A larger scale study by Snyder et al. [2013] observed widespread anisotropic patterns indicative of multiple layers. Most recently, Liddell et al. [2017] used forward modeling to characterize the nature of regional anisotropy, showing definitive evidence of dipping anisotropy beneath Baffin island, probably due to an underthrust Superior plate. Liddell et al. [2017] also presented strong evidence for a mid-lithospheric discontinuity linked to episodic craton development in Archean regions. To date, only Bastow et al. [2015] have presented body-wave tomography models of northern Hudson Bay. That study used only P-waves and lacked resolution outside of the northern Hudson Bay islands region, but resolved slower wavespeed material associated with the THO between the faster Archean cratons. Further, THO material had apparently been underthrust beneath southern Baffin Island, evidence that modern-style subduction was active at the time.

4 Methodology

4.1 Data & Networks

Our receivers come from several seismograph networks across Hudson Bay and surrounding regions, including those of the Hudson Bay Lithopheric Experiment [e.g, Bastow et al., 2015], the Portable Observatories for Lithospheric Analysis and Research Investigating Seismicity [POLARIS; e.g., Eaton et al., 2005], the Québec-Labrador Lithospheric Experiment (QUiLLE) network from the Université du Québec à Montréal, and several permanent Canadian National Seismograph Network stations (see supplementary materi-

als for a full list). All but three receivers were broadband instruments equipped with either a Güralp CMG-3ESP, CMG-3TD or Nanometrics Trillium 120PA seismometer with a flat response to 120s. Stations PINU and EUNU have response peaks at 30s, and station LG4Q is a short period instrument with only a vertical component and therefore was only used for P-wave analysis. For a given earthquake, all traces have the response of the shortest period instrument applied so that the traces will have a consistent arriving phase.

Our combined network spans ~40° degrees of longitude, and 30° of latitude from northern Ontario to Nunavut (Figure 1). The stations are most closely spaced in the Hudson Strait and western Rae craton region, with a minimum spacing of ~100 km. All earthquakes of magnitude mb ≥5.5 arriving from distances >30° from 2004 to 2015 recorded by the network were examined. Our region is poorly sampled by P-wave core phases like PKP, but well-sampled by S-wave core phases. Thus, SKS arrivals represent a significant portion of the S-wave dataset. Frederiksen et al., (2007) and Boyce et al., (2016) in the western Superior and southeast Canada regions, respectively, had similar earthquake phase coverage. After processing, 923 P/Pdiff earthquakes had a clear arriving phase; of those, 296 had enough stations responding (see Section 4.2) to include them in the final dataset (all P phases). There were 753 clear S/SKS earthquakes, with 92 meeting the criteria for number of stations responding (15 were SKS phases).

4.2 Relative Arrival Time Determination

We use the adaptive stacking (AS) method of Rawlinson and Kennett [2004] to align the recorded waveforms and then construct our relative arrival time residuals. AS works iteratively to find the time shifts needed to align each recorded trace for a given seismometer network and event. The procedure begins by first using a reference Earth model [ak135; Kennett et al., 1995] to estimate expected arrival-times; traces are first aligned to this predicted time and two initial stacks are computed. The linear and quadratic stacks are defined by:

$$V_l = \frac{1}{N}\sum_{i=1}^{N} u_i(t - t_c) \tag{1}$$

$$V_q = \frac{1}{N}\sum_{i=1}^{N} u_i(t - t_c)^2 \tag{2}$$

The stack is performed over N traces, one for each station that recorded the specific earthquake. Each trace is represented as a time series by $u_i(t)$, after the application of a time correction t_c, which is calculated from the source-receiver distance and a 1D velocity model. The traces are then stacked per equation 1 for the linear stack and equation 2 for the quadratic. The linear stack enhances the shape of the regional waveform, and the quadratic stack, since it squares the trace, emphasizes the differences between the component traces and gives a measure of the spread in waveforms.

The stacked trace V_l is then compared to each of the original traces. A new time shift, τ_i, will be applied to each trace in order for it to match the stacked, regional trace. The τ_i value for each ith trace is found by calculating a misfit between the stacked trace and the ith trace at a particular τ_i. The time shift is varied iteratively from $-x$ to $+x$ seconds (often ±1 to ±3). The value τ_i at which the lowest misfit between the trace u_i and the stacked trace V_l is then found. The misfit is calculated as a sum of the difference between the linear stacked trace and each moveout corrected trace $u_i(t)$ over the M samples in the stacking window:

$$P_p = \sum_{j=1}^{M} |V_l(t_j) - u_i(t_j - t_c^i - \tau)|^p \tag{3}$$

The p value refers to the misfit norm used to quantify the difference between the stacked trace and each station trace. We choose a p value of 3 because it penalizes small differences in time offsets from the stacked trace and thus can achieve stable results after only a few iterations [Rawlinson and Kennett, 2004]. The index 'i' represents the individual trace and the index 'j' indicates the sample within each ith trace. The result is a set of N values of τ_i. These are applied to all the traces that recorded this specific event in the network. They are then stacked again to create a new stacked trace, V_l'. The process can then be repeated and a new set of corrections can be calculated based upon the fit with the new stacked trace. This is done until the corrections stabilize. At this point the local velocity structure is assumed to be responsible for any differences from the reference model.

If the stacked signal is very similar to some particular trace then it will be clear which value of τ_i gives a minimum misfit; any deviation would cause a much poorer agreement between the two waveforms. If, on the other hand, the trace has significant noise then it may be that a variety of τ_i values give similar misfits and a clear minimum does not exist. This can be quantified by the "width", in seconds, of the time shift about the minimum τ_i before the misfit increases by some percentage X. Explicitly, the value $|T_i - \tau_i|$, such that $P(T_i) = \epsilon P(\tau_i)$, where $\epsilon = 1 + \frac{X}{100}$ [Rawlinson and Kennett, 2004]. The choice of error percentage is somewhat arbitrary, but the tomography is not very sensitive to this choice because the relative error between traces is more important. We use a value of 25% in accordance with the original choice of Rawlinson and Kennett [2004]. In practise, a minimum error must be applied, because real data have noise and there will be incoherency in the waveform across the study region. Here, this is taken to be 75% of the sampling interval for any particular earthquake. The sample rate, and thus the minimum error, is made consistent across the network by interpolating to the smallest sample interval of any of the responding stations, which is either 25 ms or 10 ms.

Figure 2 is an example event, pre and post adaptive stacking. All traces were passed through a 5 Hz low-pass filter and aligned using the ak135 model. Ten iterations of adaptive stacking were used, but most τ_i values stabilize after only five. The quadratic stack is significantly sharper, indicating the stacking procedure has reduced the spread between traces. Relative arrival-time residuals, T_{RES_i}, are then calculated by removing the mean travel-time residual from the final τ_i after all iterations.

$$T_{RES_i} = \tau_i - \frac{\sum_{j=1}^{N} \tau_j}{N} \tag{4}$$

The j-index is used instead of i in this equation to show that each ith trace has the mean from all stations $j = 1...N$ taken away. N stands for total number of receivers as before. Removing the mean has the consequence that only relative velocity structure can in principle be recovered from this method; however, it mitigates the effects of uncertainty in source origin time. This remaining time shift T_{RES} is used as input data in velocity inversions. A minimum of 20 reporting stations for P-waves, and 15 for S-waves, was required for a given earthquake to be included in our analysis.

4.3 Source-Side Effects

Several stations exhibit abrupt changes in T_{RES}, by as much as ~2s over a small backazimuth range (~315°-330°: Figure 3b,d). Local seismic structure, such as a plate-scale terrane boundary, could be responsible for such a feature at a single station, but it

is observed over most of the eastern and northern portions of our network (Figure 3a). To investigate why the abrupt T_{RES} changes are seen where they are, we considered the locations of the earthquakes that make up the feature, and their orientation to the affected stations.

At station FRB on southern Baffin Island (Figure 1), the earthquakes involved in the abrupt T_{RES} change all plot along a great circle path (GCP) from the Aleutian trench, to the tip of the Kamchatka peninsula, then south along Japan to Tokyo. Earthquakes south of Tokyo do not plot along the sharp line in the backazimuth plot (Figure 4). The earthquakes in the eastern Aleutian trench successively plot faster, 'peaking' at ~60° epicentral distance. Beyond this point earthquakes plot slower with distance. If this phenomenon concerned the specific earthquake locations, we would expect the fastest residual, or 'peak', to come from the same event for all of the affected stations in Figure 3d. This is, however, not the case, because the 'peak' event is different for each affected station (three examples are shown in Figure 4). The effect upon T_{RES} appears to instead be controlled by earthquake-receiver distance, indicating that some source-side contamination has manifested in our data. Relative arrival-time tomography assumes that the effect of source-side structure is eliminated during the calculation of the residuals when we remove the mean (Equation 4). Thus, this core assumption has been violated.

To determine whether incoming energy from the source-side affected earthquakes was systematically deflected from reference model predictions, comparisons were made with source polarization anomalies (difference between predicted and observed backazimuth) and angle of incidence anomalies (difference between predicted and observed ray parameter). However, histograms comparing anomalies between affected and unaffected stations reveal that neither parameter was correlated with the source-side effect (Figure 3b). We also examined the raypaths for the earthquakes for each of the affected stations to determine whether they followed any lithospheric terrane boundary or indicate the presence of any particular structure. No such boundary or lateral interface was found at depths up to 300 km, however (see figure of piercing points in supplemental materials). Body-wave energy from teleseismic earthquakes arrives nearly vertically at the receiver, so any receiver-side structure that could produce such wildly varying residuals would have to be present beneath every red station in Figure 3a. We consider it a more likely and simpler explanation that the structure in question affected the seismic waves close to their mutual source. The effect appears to be dependent upon source-receiver distance along subduction trench systems oriented approximately parallel to the earthquake-receiver GCP. Multi-pathing of the wavefront, which happens when the wavefront crosses itself due to complicated velocity structure, could also affect the recorded arrival times [Rawlinson et al., 2003]. However, multi-pathing is expected to be incoherent between stations [Vandecar et al., 1990], and the adaptive stacking procedure of Section 4.2 does not work on incoherent arrivals. A more plausible explanation is that the subduction zone from which the affected earthquakes emerge acts as a waveguide to energy emitted along its strike.We analyzed the seismogram frequency content of affected and unaffected rays to further test our source-side contamination hypothesis (Figure 3c). Affected seismograms display an enhancement of frequencies >1Hz, and particularly between 2 and 3 Hz, when compared to unaffected rays and to the full. This frequency characteristic is independent of whether the relative arrival-time residuals are positive or negative (Figure 3d), so the source-side structure can apparently cause P-waves to speed up and slow down. Local studies of the subduction zone in Japan have suggested that the subducted oceanic mantle lithosphere can act as a high velocity, low attenuation, waveguide [e.g., Van der Hilst and Snieder, 1996; Abers, 2005]. Early arrivals are elegantly explained in this way, but some of the source-side-affected arrivals we observe are relatively late and therefore require an alternative explanation. The thin (<10 km) layer of subducted oceanic crust beneath Japan is also known to act as a slow-velocity waveguide [e.g., Garth and Rietbrock, 2014] and can enhance high-frequency (2-3Hz) body-wave energy [e.g., Furumura and Kennett, 2008]. We speculate, therefore, that the energy arriving at the blue stations in Figure 3a has been af-

fected to some degree by the subducted plate beneath Japan, whether it be its crust, mantle lithosphere, or both.

We tested the pervasiveness of the source-side T_{RES} feature with parallel datasets consisting of fewer stations: a 'Small Model' eliminating the northern and southern-most receivers, an 'East Model' using only stations from Southampton Island and eastward, and a 'West Model' using only stations from Southampton Island and westward (Figure 5). The effect was much more pronounced for the P-waves rather than the S-waves so this analysis was restricted to the P-wave dataset. Note that all data were completely re-stacked in each subset. This is necessary because the regional mean may change every time a receiver is removed from the network.

The results of re-stacking the smaller model space data shows that the source-side T_{RES} feature is effectively eliminated for the smaller models (side panels of Figure 5): the peak-to-peak spread for the two representative stations has reduced from ±1s to ±0.5s. The implication is that the source-side effect does not cause significant variations in data over a smaller network area and the T_{RES} feature is therefore eliminated by removing the regional mean in Equation 4. Network apertures >1200 km may therefore be prone to source-side structure contamination, at least from subduction zones oriented parallel to the GCP. We can contribute only one network-source region observation, so we cannot confidently constrain the degree of alignment between GCP and subduction zone strike at which contamination of the receiver-side residuals begins. Careful examination of the orientation of subduction zones from source regions relative to the network should be considered, and input data should aways be examined closely before inversion. We re-visit this issue, including how and whether it affects our inversions, in Section 5.1.

4.4 Tomographic Inversion Procedure

4.4.1 FMTOMO

The inversion code used in this study is the Fast Marching TOMOgraphic (FMTOMO) method of Rawlinson et al. [2006] to solve for upper mantle seismic structure. Two grids of nodes are defined to make up the model space. The velocity grid is made of the unknowns in the inversion that control the velocity field, and the propagation grid is used to track the wave field through the model space during the forward step of the inversion. FMTOMO uses the Tau-P method (Kennett and Engdahl, 1991) to compute ray traveltimes from the source to the edge of the local 3-D model region, and then applies a grid-based eikonal solver, known as the Fast Marching Method, to track wavefronts with a propagation grid to the surface through velocity structure which may vary radially and laterally. This propagation grid is not used to define the model, but simply represents a discrete sampling at some specified resolution. During inversion FMTOMO minimizes the objective function:

$$S(m) = \frac{1}{2}[\Psi(m) + \epsilon\Phi(m) + \eta\Omega(m)] \tag{5}$$

The value m refers to the model parameters that are changed during the inversion. The first term, $\Psi(m)$, is minimized when the model travel times match as closely as possible the observed travel times. The second term $\Phi(m)$ penalizes models that differ from the reference or starting model m_0. The third term, $\Omega(m)$, penalizes model roughness. The regularization terms, η and ϵ, control damping (similarity to starting model) and smoothing (degree of model roughness) respectively. Ideally, we seek a model that satisfies the data but is also smooth and as close to the starting model as possible.

Through extensive testing of the model space we determined the regularization parameters via trade-off curve analysis that balanced data fit with model roughness. The 'residual' value in Figure 6 is a measure of how much of the input data is unexplained

by the model; a low residual means a higher data fit. A high data fit may require an unrealistically rough model, and an overly smooth model may miss important structure. Typically, the parameters that produce the 'knee' of a tradeoff curve between roughness and data misfit are understood to be the best choice. We produced inversions of the input data for every combination of a sequence of both smoothing and damping values of 0.1-100. When plotted together, these give a tradeoff area rather than a single curve. The centre point of the tradeoff area is chosen for the final model inversions (Figure 6).

4.4.2 Crustal Modeling

Moho topography and crustal velocity structure can have a significant influence on teleseismic travel times [e.g., Waldhauser et al., 2002]. To mitigate this problem, we applied a crustal velocity and Moho model developed from receiver function and surface wave inversion results [Gilligan et al., 2016]. Moho topography in northern Hudson Bay is significant; ~7 km deeper beneath Baffin Island than the Archean regions to the west [e.g., Thompson et al., 2010]. Moho depth estimates from Gilligan et al. [2016] at each station were interpolated to produce a continuous interface and inserted into the initial FMTOMO model space. Likewise, the modeled crustal velocity values were sampled every 2 km beneath each station and interpolated to create a layer with its base defined by the Moho model. Data fitting was best when the crustal models of Gilligan et al. [2016] were fixed in our inversions rather than allowed to vary.

4.4.3 Resolution Testing

To test the resolving ability of our dataset we performed synthetic checkerboard resolution tests. The predicted arrival times for our earthquakes are calculated through a model space with ±0.4 km/s checkers (relative to ak135). We then use those predicted times as input data for an inversion. This test attempts to give a realistic visualization of where the dataset can recover velocity anomalies, and what size of anomaly might be resolvable. Our network has variable station spacing, the shortest being 100-200 km in the Hudson Strait, southern Baffin Island and the eastern Rae domain. The input checkers in Figure 7 are ~300x300 km horizontally, and are120 km thick, but vary slightly with latitude. This length-scale governs the minimum size of feature that can be resolved by this model in regions of minimum station coverage.

The recovered inversion model in Figure 7 can be compared to the input checkerboard model to see where we have good resolution and the degree to which anomalies are smeared. The grey mask excludes regions of the model space where no ray paths travel. Model recovery is similar for P and S wave models, although the P recovery is everywhere better, with best resolution along the Hudson Strait and northern islands region (transect B-B*: Figure 7). Other regions, especially central Hudson Bay itself, have relatively poor resolution due to a lack of stations and the near-vertical incidence of teleseismic arrivals. Vertical smearing is low in the central portions of the model, and worst near the edges of the model space where fewer crossing rays can be expected. Vertical smearing like this is typical of tomography studies because the energy from teleseismic earthquakes arrives nearly vertically beneath the receivers.

5 Results

5.1 Source-Side Structure in Inversions

Before interpreting our results in terms of Hudson Bay upper mantle seismic structure, we must determine how the source-side structure problems identified in Section 4.3 (Figures 3,4) affect our models. Specifically, we forward model travel-times in the top 300 km and, separately, the bottom 300 km of our tomographic model, then compare synthetic and observed travel-time residuals. This lets us test whether spurious structure is mapped

into the upper portions of our model where we make structural interpretations, or whether it falls into the deeper, less-well-resolved and un-interpreted parts. The results are shown for three example stations, FRB, LG4Q, and LAIN (matching Figure 3) because their wide spacing illustrates the pervasiveness of the effect.

Our full model space extends to 800 km depth. Residuals calculated with only the bottom 300 km of the inverted model region active accommodate much of the source-side feature (Figure 8). The model with only the top 300 km of the model space active has no indication of the source-side feature. This indicates that the inversion code is placing structure to explain the source-side contaminated data in the less-constrained, deepest 300 km of the model space. We can thus safely interpret structure in the upper 500 km of the full model. Parameterizing tomographic models deeper than the resolving power of the teleseismic dataset is common [e.g., Vandecar et al., 1995; Villemaire et al., 2012]. Our work demonstrates this approach is particularly important for large aperture (>1000 km) networks.

5.2 P and S-Wave Inversion Models

The P and S wave tomographic models in Figures 9 and 10 show significant heterogeneous mantle wavespeed structure in northern Hudson Bay and Nunavut. The depth slices are presented at a mid-lithospheric depth of 150 km, and depth variation is shown via the cross-sections. The Quebec-Baffin transect (cross-section A-A*) reveals slow wavespeed structure extending to at least 500 km in the Hudson Strait, with faster wavespeeds in the Superior craton to the south and the Churchill to the north for both P and S waves. A laterally robust slow wavespeed curtain extending east-west through the northern portion of Hudson Bay (cross-section B-B*), then turning northwards towards the east coast of southern Baffin Island, is also imaged in both models. The western portion of the B-B* cross-section is fast in the P-wave model, but appears slow in the S-wave model. Just northward, within our station coverage, both P and S-wave models in Figure 9 image a low wavespeed anomaly on Southampton Island in the centre of the model space. The S-wave model (Figure 9b) sees this anomaly extend southward where it intersects with the B-B* transect, while the P-wave model does not (Figure 9a). This discrepancy is less likely due to actual structural variations and more likely a result of the model being under-constrained due to a lack of stations in the central part of Hudson Bay. A sharp, vertical change in seismic wavespeed occurs beneath Southampton Island (cross-section C-C*) in the P-wave model, with a similar, although less-pronounced, feature in the S-wave model. This is as strong an anomaly as the THO-related feature to the east.

Our inversion model has resolution in the Archean central Rae and Hearne cratons (Figure 7) and results indicate a complex and heterogeneous velocity pattern within the shield region. There exists a low velocity anomaly (north end of C-C* in Figure 9) near the connection of Melville Peninsula to the main Rae landmass (Figure 1), and its shape differs between the P and S-wave models more substantially than anomalies to the east beneath Hudson Bay and Baffin Island.

The inversion models discussed in this section were created using the entire dataset. P-wave inversion models for each of the subsets, ‘Small Model’, ‘East Model’, and ‘West Model’, are included in the supplementary materials. Each subset’s inversion model differs slightly from the larger model due to the lower resolving power of the smaller network, but they all share the same first order characteristics where they overlap spatially. This provides support for the robustness of the anomalies shown in in Figures 9 and 10.

6 Discussion

6.1 Causes of Seismic Heterogeneity & Comparison to Previous Tomographic Studies

As explained in Section 3, global models of Hudson Bay seismic structure have imaged uniformly fast wavespeeds in the upper ~250km of the mantle. Our relative arrival-time inversion approach constrains heterogeneities with respect to a regional, not global, mean, however. For example, the mean S-wave velocity anomaly at permanent station FRB in the global model of Ritsema et al. [2011] is $\delta V_S \approx 2.5\%$. However, the mean relative arrival time residual for FRB in our study is near zero (0.2s), meaning both high and low velocity anomalies in our models (Figures 9 and 10) are likely fast compared to the global mean and thus reflect wavespeed heterogeneity within the Canadian Shield [Bastow, 2012].

Surface erosion of cratonic regions like northern Hudson Bay results in loss of radiogenic particles and therefore an anomalously low heat flow [$\leq$50 mW/m^2, e.g., Levy et al., 2010]. Fast wavespeed cratonic roots or keels are thus often considered >200°C cooler than surrounding, younger terranes [e.g., Mareschal et al., 2004]. Elevated mantle temperatures and associated partial melt can cause low seismic wavespeeds [e.g., Allen et al., 2002; Bastow et al., 2008], but are inappropriate hypotheses for seismic heterogeneity in our study area since it is thought to be cooler than average at upper mantle depths [Goes and van der Lee, 2002]. Anisotropy may also influence wave speed variations in northern Hudson Bay (e.g. Darbyshire et al., 2013; Liddell et al., 2017). However, the general consistency between our P wave and S wave models (Figures 9 and 10) despite approximately perpendicular particle motion between the phases, and our good back-azimuthal coverage of earthquakes (Figure 1), implies that this is not a predominant factor, and that our models are dominated by isotropic wavespeed variations. Our tomographic images, with their higher lateral resolving power than earlier surface wave studies, illuminate the finer-scale internal architecture of the northern Hudson Bay region. Other relative arrival time studies of nearby regions [e.g., Frederiksen et al., 2013; Boyce et al., 2016] included terranes or geological features that ranged in age from Archean to Phanerozoic. The peak-to-peak residual amplitudes of studies like these are to some degree set by the age range of the structures within the model space. Our study, in contrast, spans only Precambrian lithosphere and thus our models tend to highlight internal variations in Precambrian lithospheric structure rather than the typically more pronounced contrasts between Precambrian and Phanerozoic lithosphere.

The eastern edge of southern Baffin Island in our models exhibits a low velocity anomaly for both P and S waves at lithospheric depths. S-wave perturbations at 150 km depth in the continent-scale model of Schaeffer and Lebedev [2014] show a sharp boundary to the cratonic lithosphere in this region, following closely the eastern coast of Baffin Island. Lithospheric thinning in this area has occurred since the opening of Baffin Bay separating Canada from Greenland in the late Jurassic to early Cretaceous [Larsen et al., 1999; **?**]. Our models are therefore imaging the edge of low velocity material associated with the asthenosphere at the Churchill craton's edge.

6.2 Mantle Seismic Structure of the Churchill Plate

With acceptable resolution for much of the central Rae and northern Hearne domains (Figure 7), we image considerable seismic heterogeneity throughout the Churchill plate. Our study may be expected to image seismic variation that has not previously been resolved by global studies because of our greater number of stations and better data coverage. Surface wave studies also have naturally low lateral resolution compared to teleseismic body wave tomography.

Marked seismic heterogeneity within Precambrian domains has been observed worldwide (e.g., Fennoscandia, Bannister et al. [1991]; China, Tian et al. [2009]; Australia, Fishwick and Rawlinson [2012]). Internal cratonic velocity variations of the southern African Kaapvaal craton were observed to be very small (~0.5%), however, low velocity anomalies were modeled within the eastern edge of the Kaapvaal craton [Fouch et al., 2004; Youssof et al., 2015]. Called the Bushveld Complex, this anomaly has been associated with ~2.0 Ga Proterozoic chemical modification and mantle refertilization [James et al., 2001; Youssof et al., 2015]. Similar examples of cratonic collisions initiating metasomatism and creating fertile, low-velocity mantle regions include Siberia [Griffin et al., 2005], and the central Superior province [Boyce et al., 2016].

The seismic velocity variations in our region are not easily explained by age: the boundary between the Paleoarchean Rae and the Mesoarchean Hearne cratons (STZ) is not correlated with a consistent change in wavespeed at lithospheric depths (Figure 11). While a number of faults and gravity gradients have been defined in the central Rae craton [e.g., Snyder et al., 2015], we do not observe mantle expression or correlation to any of these delineations within either the P or S wave models (Figures 9 and 10). Diamondiferous kimberlites are expected to correlate with thick lithosphere and therefore fast velocity anomalies; however, our models show no obvious correlation with diamond prospects (Figure 1). Magnetotelluric studies within the western Hearne in Alberta and in the Yellowknife Fault Zone in the Yukon, also attributed upper mantle conductive anomalies to widespread metasomatism [Nieuwenhuis et al., 2014; Jones and Garcia, 2006].

The Hudson Plutons are 1.85-1.81Ga intrusive granites interpreted as post-orogenic lower crustal intrusions hosting crustal melt or metasomatic materials found throughout the Churchill domain but concentrated near the west coast of northern Hudson Bay near Melville Peninsula [Figure1; Berman et al., 2005; Peterson, 2002]. They are associated with a Bouger gravity anomaly low and near-vertical conductive anomalies imaged with magnetotellurics interpreted to be carbon films or leftover water [Spratt et al., 2014]. These inversions also showed that upper mantle resistivity changed significantly between various lithospheric blocks, increasing from Baffin Island south to the STZ. Consistent with earlier geological work [e.g., Hynes & Rivers, 2010], Boyce et al. [2016] interpreted slower-than-expected wavespeeds beneath the Grenville Front as evidence for metasomatic modification of the Superior lithosphere during the 250 Ma subduction process. The resulting wavespeed anomalies are of the order of ±1.5%, significantly smaller than those we observe (~4% below Melville peninsula). As far as we have could determine, no petrological studies have claimed large-scale metasomatic modification of the Melville lithosphere. Therefore, since THO tectonism acted for a much shorter period (~80Ma) than during the Grenville orogen, we consider metasomatism only partially capable of explaining our velocity anomalies. The remainder of the anomalous structure likely reflects inherent compositional differences between lithospheric blocks, un-related to metasomatic modification. We interpret our Rae anomaly (Figures 9 and 10) to reflect a combination of metasomatism and compositional differences between constituent lithospheric blocks; the metasomatism being driven by the same forces that created the crustal melts of the Hudson plutons.

6.3 Mantle Seismic Structure of the Trans-Hudson Orogen & Implications for Precambrian Plate Tectonics

A striking feature in Figures 9 and 10 is the strong slow wavespeed feature that curves around the Quebec mainland and through the Hudson Strait, then angles northeast beneath the Archean crust of southern Baffin Island (B-B*). Gilligan et al. [2016] found compelling similarities between the crustal velocities of the Tibetan Plateau and southern Baffin Island, allowing for ~30 km of erosion since completion of the THO. Recent modeling of seismic anisotropy using backazimuthal variation of shear-wave splitting parameters in southern Baffin Island strongly suggested the presence of dipping anisotropy, and

related that to subducted material from the THO [Liddell et al., 2017]. These geophysical studies support a growing number of geological studies that consider the THO reminiscent of a modern-style subduction zone [e.g., St-Onge et al., 2009; Weller and St-Onge, 2017]. Our tomographic inversions clearly image low velocity material from the THO that extends beneath the Archean terranes of southern Baffin Island (A-A* in Figures 9 and 10). We interpret this anomaly as being due to compositionally distinct Proterozoic material underthrust beneath the Archean Churchill craton during the THO in a modern-style tectonic collision.

A further strong velocity contrast manifests near Southampton Island in both P and S wave models (Figures 9 and 10). Higher velocities in the east give way to lower velocities to the northwest into the Rae domain. Considering the interpretation of plate tectonic activity, this contrast is most likely due to a lithospheric boundary from an Archean micro-continent, caught in between the Churchill and the Superior during the THO. Interpretations of a terrane boundary in this region were also made from SKS splitting [Liddell et al., 2017] and magnetotelluric data [Spratt et al., 2012]; however, Gilligan et al. [2016] found no clear difference in crustal structure between the various northern Hudson Bay islands. This indicates either alteration of the mantle or underthrusting of mantle material from a nearby terrane beneath Southampton Island. A possible candidate for this is the Sugluk block, a Mesoarchean terrane of high grade metamorphic rocks considered distinct from its surrounding blocks due to a lack of 2.5-2.6 Ga magmatism [e.g., Hoffman, 1985; Corrigan et al., 2009]. The Sugluk is exposed on the northwestern tip of Quebec where it is intruded by plutonic rocks of the Narsajuaq arc [e.g., Dunphy and Ludden, 1998; St-Onge et al., 2002]. Bouger gravity and aeromagnetic signatures indicate that it extends north to Baffin Island and west beneath Hudson Bay into the region where we observe the velocity interface [Corrigan et al., 2009].

The Snowbird Orogeny took place during the initiation of the THO and ended <0.1 Ga before terminal collision of the Superior and Churchill [Berman et al., 2007; Corrigan et al., 2009]. The result was the >2800 km long suture zone between the Rae and the Hearne domains. Cross sections of the P and S-wave model in Figure 11 show no consistent mantle velocity distinction between the domains divided by the STZ. Neither have studies of lithospheric anisotropy found evidence for fabrics that parallel any potential tectonic boundary at the STZ [e.g., Snyder et al., 2013; Liddell et al., 2017]. However, the lack of stations south of the STZ means we cannot provide a more detailed discussion of its structure. Our results are most consistent with an interpretation of the STZ as a relatively minor event involving what might be considered a tributary of the much larger Manikewan ocean whose closure initiated the THO [Corrigan et al., 2009]. This process brought together two blocks that were of relatively similar composition from a seismic wavespeed perspective, and on too small a scale to create the features we image for the THO to the east.

7 Conclusions

We have presented new P and S-wave tomographic inversions for the northern Hudson Bay region of Canada using a combined network of temporary and permanent broadband seismograph stations. Our results constitute the most comprehensive body-wave tomographic model of northern Hudson Bay to date.

We have shown that sources with raypaths approximately parallel to subduction zones may include some source-side influence after relative-arrival processes and removal of the mean. We further show that this effect can be mitigated to some degree by limiting network size and carefully examining where spurious structure may be mapped into the inversion. Nevertheless, our work shows that source-network orientations and backazimuth residual patterns should be closely examined to ensure that the results truly represent only local structure.

The Archean Rae and Hearne domains exhibit complex internal structure, implying a complex accretionary history. However, there is no seismic velocity evidence for a terrane boundary across the Snowbird Tectonic Zone (Rae-Hearne suture), consistent with the view that it was a relatively short-lived orogeny of modest scale.

A strong velocity contrast at shallow depths on and around Southampton Island in northern Hudson Bay is interpreted as a micro-continent (Sugluk block) with a collisional history distinct from the Churchill plate to the north and the Superior plate to the south.

We interpret slow wavespeeds between the Superior and Churchill plates as Paleoproterozoic THO material caught between the Archean colliders as part of a modern-style plate tectonic event. Low velocity anomalies persist beneath the Churchill province, but not beneath the Archean Superior province. We interpret this as strong evidence for 1.8 Ga Paleoproterozoic plate-scale underthrusting.

Acknowledgments

The authors would like to thank A. Boyce, L. Petrescu, and C. Ogden of the ICcratons group as well as S. Goes for numerous enlightening conversations about Canadian Precambrian geology and beyond. M.V. Liddell is funded by an Imperial College President's Scholarship. F.A. Darbyshire is supported by the Natural Sciences and Environment Research Council of Canada through their Discovery Grant and Canada Research Chair programmes. The data used in this study are available for download via POLARIS or the IRIS DMC, and the processed relative arrival time dataset is available for download in as a digital supplement. Further questions can be directed to M.V. Liddell (m.liddell14@imperial.ac.uk).

References

Abers, G. A., 2005. Seismic low-velocity layer at the top of subducting slabs: Observations, predictions, and systematics. *Physics of the Earth and Planetary Interiors*, 149, 7–29

Abt, D. L., Fischer, K. M., French, S. W., Ford, H. A., Yuan, H., Romanowicz, B., 2010. North American lithospheric discontinuity structure imaged by Ps and Sp receiver functions. *Journal of Geophysical Research: Solid Earth* 115 (9), 1–24

Allen, R. M., Nolet, G., Morgan, W. J., Vogfjörd, K., Bergsson, B. H., Erlendsson, P., Foulger, G. R., Jakobsdóttir, S., Julian, B. R., Pritchard, M., Ragnarsson, S., Stefánsson, R., 2002. Imaging the mantle beneath Iceland using integrated seismological techniques. *Journal of Geophysical Research: Solid Earth* 107 (B12), 16p

Bannister, S. C., Ruud, B. O., Husebye, E. S., 1991. Tomographic estimates of sub-Moho seismic velocities in Fennoscandia and structural implications. *Tectonophysics* 189 (1-4), 37–53

Bao, X., Eaton, D. W., 2015. Large variations in lithospheric thickness of western Laurentia: Tectonic inheritance or collisional reworking? *Precambrian Research* 266, 579–586

Bastow, I. D., Nyblade, A. A., Stuart, G. W., Rooney, T. O., Benoit, M. H., 2008. Upper mantle seismic structure beneath the Ethiopian hot spot: Rifting at the edge of the African low-velocity anomaly. *Geochemistry, Geophysics, Geosystems* 9 (12), 25 p

Bastow, I. D., Kendall, J. M., Helffrich, G. R., Thompson, D. A., Wookey, J., Brisbourne, A. M., Hawthorn, D., Eaton, D. W., Snyder, D. B., 2011. The Hudson Bay Lithospheric Experiment. *Astronomy and Geophysics* 52 (6), 21–24

Bastow, I. D.,2012. Relative arrival-time upper-mantle tomography and the elusive background mean. *Geophysical Journal International* 190 (2), 1271–1278

Bastow, I. D., Eaton, D. W., Kendall, J.-M., Helffrich, G., Snyder, D. B., Thompson, D. A., Wookey, J., Darbyshire, F. A., Pawlak, A. E., 2015. The Hudson Bay Lithospheric Experiment (HuBLE): insights into Precambrian plate tectonics and the development of mantle keels. *Geological Society, London, Special Publications* 389, 41–67

Berman, R. G., Davis, W. J., Pehrsson, S., 2007. Collisional Snowbird tectonic zone resurrected: Growth of Laurentia during the 1.9 Ga accretionary phase of the Hudsonian orogeny. *Geology* 35 (10), 911–914

Berman, R. G., Sanborn-Barrie, M., Stern, R. A., Carson, C. J., 2005. Tectonometamorphism at ca. 2.35 and 1.85 Ga in the Rae domain, western Churchill Province, Nunavut, Canada: insights from structural, metamorphic and in situ geochronological analysis of the southwestern Committee Bay belt. *The Canadian Mineralogist* 43 (1), 409–442

Boyce, A., Bastow, I. D., Darbyshire, F. A., Ellwood, A. G., Gilligan, A., Menke, W., 2016. Subduction Beneath Laurentia Modified the North American Craton Edge : Evidence from P and S-wave Tomography. *Journal of Geophysical Research: Solid Earth* 121, 5013–5030

Bruneton, M., Pedersen, H. A., Farra, V., et al., 2004. Complex lithospheric structure under the central Baltic Shield from surface wave tomography. *Journal of Geophysical Research: Solid Earth* 109 (B10), 1–15

Corrigan, D., Pehrsson, S., Wodicka, N., de Kemp, E., 2009. The Palaeoproterozoic Trans-Hudson Orogen: a prototype of modern accretionary processes. *Geological Society, London, Special Publications* 327 (1), 457–479

Darbyshire, F. A., Eaton, D. W., 2010. The lithospheric root beneath Hudson Bay, Canada from Rayleigh wave dispersion: No clear seismological distinction between Archean and Proterozoic mantle. *Lithos* 120 (1-2), 144–159

Darbyshire, F. A., Eaton, D. W., Bastow, I. D., 2013. Seismic imaging of the lithosphere beneath Hudson Bay: Episodic growth of the Laurentian mantle keel. *Earth and Planetary Science Letters* 373, 179–193

Davis, W. J., Hanmer, S., Tella, S., Sandeman, H. A., Ryan, J. J., 2006. U-Pb geochronology of the MacQuoid supracrustal belt and Cross Bay plutonic complex: Key components of the northwestern Hearne subdomain, western Churchill Province, Nunavut, Canada. *Precambrian Research* 145 (1-2), 53–80

Dunphy, J. M., Ludden, J. N., 1998. Petrological and geochemical characteristics of a Paleoproterozoic magmatic arc (Narsajuaq terrane, Ungava Orogen, Canada) and comparisons to Superior Province granitoids. *Precambrian Research* 91 (1-2), 109–142

Eaton, D. W., Adams, J., Asudeh, I., Atkinson, G. M., Bostock, M. G., Cassidy, J. F., Ferguson, I. J., Samson, C., Snyder, D. B., Tiampo, K. F., Unsworth, M. J., 2005. Investigating Canada's Lithosphere and earthquake hazards with portable arrays. *Eos, Transactions American Geophysical Union* 86 (17), 169

Fishwick, S., Rawlinson, N., 2012. 3-D structure of the Australian lithosphere from evolving seismic datasets. *Australian Journal of Earth Sciences* 59 (6), 809–826

Fouch, M. J., James, D. E., VanDecar, J. C., van der Lee, S., 2004. Mantle seismic structure beneath the Kaapvaal and Zimbabwe Cratons. *South African Journal of Geology* 107 (1-2), 33–44

Frederiksen, A. W., Miong, S. K., Darbyshire, F. A., Eaton, D. W., Rondenay, S., Sol, S., 2007. Lithospheric variations across the Superior Province, Ontario, Canada: Evidence from tomography and shear wave splitting. *Journal of Geophysical Research: Solid Earth*, 112 (7), 20 p

Frederiksen, A. W., Bollmann, T., Darbyshire, F., Van Der Lee, S., 2013. Modification of continental lithosphere by tectonic processes: A tomographic image of central North America. *Journal of Geophysical Research: Solid Earth*, 118 (3), 1051-1066

Furumura, T., Kennett, B., 2008. A Scattering Waveguide in the Heterogeneous Subducting Plate. *Advances in Geophysics*, Ch. 7 (50), 195–217

Garth, T., Rietbrock, A., 2014. Downdip velocity changes in subducted oceanic crust beneath Northern Japan-insights from guided waves. *Geophysical Journal International*, 198 (3), 1342–1358

Gibb, R. A., 1983. Model for suturing of Superior and Churchill plates: an example of double indentation tectonics. *Geology* 11 (7), 413–417

Gilligan, A., Bastow, I. D., Darbyshire, F. A., 2016. Seismological structure of the 1.8 Ga Trans-Hudson Orogen of North America. *Geochemistry Geophysics Geosystems* 17, 2421–2433

Goes, S., van der Lee, S., 2002. Thermal structure of the North American uppermost mantle inferred from seismic tomography. *Journal of Geophysical Research*, 107, 13p

Griffin, W. L., Natapov, L. M., O'Reilly, S. Y., van Achterbergh, E., Cherenkova, A. F., Cherenkov, V. G., 2005. The Kharamai kimberlite field, Siberia: Modification of the lithospheric mantle by the Siberian Trap event. *Lithos* 81 (1-4), 167–187

Hawkesworth, C. J., Cawood, P. A., Dhuime, B., Kemp, T. I. S., 2017. Earth's Continental Lithosphere Through Time. *Annual Review of Earth and Planetary Sciences* 45, 169–198

Hoffman, P. F., 1985. Is the Cape Smith Belt (northern Quebec) a klippe? *Canadian Journal of Earth Sciences* 22, 1361–1369

Hoffman, P. F., 1988. United Plates of America, the Birth of a Craton: Early Proterozoic Assembly and Growth of of Laurentia. *Annual Review of Earth and Planetary Sciences* 16, 543–603

Hopkins, M., Harrison, T. M., Manning, C. E., 2008. Low heat flow inferred from >4 Gyr zircons suggests Hadean plate boundary interactions. *Nature* 456 (7221), 493–496

Hynes, A., Rivers, T., 2010. Protracted continental collision - evidence from the Grenville Orogen *Canadian Journal of Earth Sciences* 47, 591–620

Kennett, B. L.N., Engdahl, E. R., 1991. Traveltimes from global earthquake location and phase identification. *Geophysical Journal International* 105 (2), 429–465

Kennett, B. L.N., Engdahl, E. R., Buland, R, M., 1995. Constraints on seismic velocities in the Earth from Traveltimes. *Geophysical Journal International* 122 (1), 108–124

James, D. E., Fouch, M. J., VanDecar, J. C., van der Lee, S., the Kaapvaal Seismic Group, 2001. Tectospheric structure beneath southern Africa. *Geophysical Research Letters* 28 (13), 2485–2488

Jones, A., 2002. Magnetotelluric and teleseismic study across the Snowbird Tectonic Zone, Canadian Shield: A Neoarchean mantle suture? *Geophysical Research Letters* 29 (17), 17–20

Jones, A.G., Garcia, X., 2002. Electrical resistivity structure of the Yellowknife River Fault Zone and surrounding region, in Gold in the Yellowknife Greenstone Belt, Northwest Territories: Results of the EXTECH III Multidisciplinary Research Project. Special Publication No. 3, pp. *Geological Association of Canada, Mineral Deposits Division Chap. 10*, St. John's, Newfoundland, Canada, 126–141.

Larsen, L. M., Rex, D. C., Watt, W. S., Guise, G. G., 1999. ^{40}Ar-^{39}Ar dating of alkali basaltic dykes along the south-west coast of Greenland: Cretaceous and Tertiary igneous activity along the eastern margin of the Labrador Sea. *Geology of Greenland Survey Bulletin*, 184, 19–29

Lebedev, S., Van Der Hilst, R. D., 2008. Global upper-mantle tomography with the automated multimode inversion of surface and S-wave forms. *Geophysical Journal International* 173 (2), 505–518

Levy, F., Jaupart, C., Mareschal, J. C., Bienfait, G., Limare, A., 2010. Low heat flux and large variations of lithospheric thickness in the Canadian Shield. *Journal of Geophysical Research: Solid Earth* 115 (6), 1–23

Li, C., van der Hilst, R. D., Engdahl, E. R., Burdick, S., 2008. A new global model for P wave speed variations in Earth's mantle. *Geochemistry, Geophysics, Geosystems* 9 (5), 21 p

Liddell, M. V., Bastow, I. D., Darbyshire, F. A., Gilligan, A., Pugh, S., 2017. The formation of Laurentia: Evidence from shear wave splitting. *Earth and Planetary Science Letters* 479, 170–178

Mareschal, J. C., Nyblade, A., Perry, H. K., Jaupart, C., Bienfait, G., 2004. Heat flow and deep lithospheric thermal structure at Lac de Gras, Slave Province, Canada. *Geophysical Research Letters* 31 (12), 2–5

Nieuwenhuis, G., Unsworth, M. J., Pana, D., Craven, J., Bertrand, E., 2014. Three-dimensional resistivity structure of Southern Alberta, Canada: implications for Precambrian tectonics. *Geophysical Journal International* 197 (2), 838–859

Oakey, G. N., Chalmers, J. A., 2014. A new model for the Paleogene motion of Greenland relative to North America: Plate reconstructions of the Davis Strait and Nares Strait regions between Canada and Greenland. *Journal of Geophysical Research: Solid Earth* 119 (B10401), 360–363

Pawlak, A., Eaton, D. W., Bastow, I. D., Kendall, J. M., Helffrich, G., Wookey, J., Snyder, D. B., 2011. Crustal structure beneath Hudson Bay from ambient-noise tomography: Implications for basin formation. *Geophysical Journal International* 184 (1), 65–82

Pawlak, A., Eaton, D. W., Darbyshire, F. A., Lebedev, S., Bastow, I. D., 2012. Crustal anisotropy beneath Hudson Bay from ambient noise tomography: Evidence for post-orogenic lower-crustal flow? *Journal of Geophysical Research: Solid Earth* 117, 1–16

Petrescu, L., Darbyshire, F. A., Bastow, I. D., Totten, E., Gilligan, A., 2017. Seismic anisotropy of Precambrian lithosphere: Insights from Rayleigh wave tomography of the eastern Superior Craton *Journal of Geophysical Research: Solid Earth* 122, 3754-3775

Peterson, T. D., Van Breemen, O., Sandeman, H. A., Cousens, B., 2012. Proterozoic (1.85-1.75 Ga) igneous suites of the Western Churchill Province: Granitoid and ultrapotassic magmatism in a reworked Archean hinterland *Precambrian Research*, 119, 73–100

Porritt, R. W., Miller, M. S., Darbyshire, F. A., 2015. Lithospheric architecture beneath Hudson Bay. *Geochemistry, Geophysics, Geosystems* 16 (7), 2262–2275

Rawlinson, N., Sambridge, M., 2003. Seismic Traveltime Tomography of the Crust and Lithosphere. *Advances in Geophysics*, 46, 81–197

Rawlinson, N., de Kool, M., Sambridge, M., 2006. Seismic wavefront tracking in 3D heterogeneous media: applications with multiple data classes. *Exploration Geophysics* 37 (4), 322–330

Rawlinson, N., Kennett, B., 2004. Rapid estimation of relative and absolute delay times across a network by adaptive stacking. *Geophysical Journal International* 157, 332–340

Rawlinson, N., Spakman, W., 2016. On the use of sensitivity tests in seismic tomography. *Geophysical Journal International* 205 (2), 1221–1243

Ritsema, J., Deuss, A., Van Heijst, H. J., Woodhouse, J. H., 2011. S40RTS: A degree-40 shear-velocity model for the mantle from new Rayleigh wave dispersion, teleseismic traveltime and normal-mode splitting function measurements. *Geophysical Journal International* 184 (3), 1223–1236

Rogers, J. J., Santosh, M., 2002. Configuration of Columbia, a Mesoproterozoic Supercontinent. *Gondwana Research* 5 (1), 5–22

Rychert, C. A., Shearer, P. M., 2009. A Global View of the Lithosphere-Asthenosphere Boundary. *Science* 324, 495–498

Sandoval, S., Kissling, E., Ansorge, J., 2004. High-resolution body wave tomography beneath the SVEKALAPKO array - II. Anomalous upper mantle structure beneath the central Baltic Shield. *Geophysical Journal International* 157 (1), 200–214

Schaeffer, A. J., Lebedev, S., 2013. Global shear speed structure of the upper mantle and transition zone. *Geophysical Journal International* 194 (1), 417–449

Schaeffer, A. J., Lebedev, S., 2014. Imaging the North American continent using waveform inversion of global and USArray data. *Earth and Planetary Science Letters* 402 (C), 26–41

Shapiro, N. M., Ritzwoller, M. H., 2002. Monte-Carlo inversion for a global shear-velocity model of the crust and upper mantle. *Geophysical Journal International* 151 (1), 88–105

Skulski, T., Sandeman, H. A., Machattie, T., Young, M., Carson, C., Berman, R. G., Brown, J., Rayner, N., Panagapko, D., Byrne, D., Deyell, C., 2003. Bedrock geology of the Ellice Hills map area and new constraints on the regional geology of the Committee Bay area, Nunavut. *Geological Survey of Canada, Current Research*, 2003-C22

Snyder, D. B., Berman, R. G., Kendall, J. M., Sanborn-Barrie, M., 2013. Seismic anisotropy and mantle structure of the Rae craton, central Canada, from joint interpretation of SKS splitting and receiver functions. *Precambrian Research*, 232, 189–208

Snyder, D. B., Craven, J. A., Pilkington, M., Hillier, M. J., 2015. The 3-dimensional construction of the Rae craton, central Canada. *Geochemistry Geophysics Geosystems*, 16 (1-2), 3555–3574

Snyder, D. B., Humphreys, E., Pearson, D. G., 2017. Construction and destruction of some North American cratons. *Tectonophysics*, 694, 464-485

Sol, S., Thomson, C. J., Kendall, J. M., White, D., VanDecar, J. C., Asudeh, I., 2002. Seismic tomographic images of the cratonic upper mantle beneath the Western Superior Province of the Canadian Shield - A remnant Archean slab? *Physics of the Earth and Planetary Interiors*,134 (1-2), 53–69

Spratt, J. E., Skulski, T., Craven, J. A., Jones, A.G., Snyder, D. B., Kiyan, D., 2014. Magnetotelluric investigations of the lithosphere beneath the central Rae craton, mainland Nunavut, Canada. *Journal of Geophysical Research: Solid Earth*, 119, 2415–2439

Spratt, J. E., Craven, J. A., Sanborn-Barrie, M., 2012. Southampton Island Magnetotelluric Survey: Data Acquisition and Preliminary Analysis. *Geological Survey of Canada, Open File 6988*, 39 p

St-Onge, M. R., Scott, D. J., Wodicka, N., 2002. Review of crustal architecture and evolution in the Ungava Peninsula - Baffin Island area: connection to the Lithoprobe ECSOOT transect. *Canadian Journal of Earth Sciences*, 39 (5), 589–610

St-Onge, M. R., Searle, M. P., Wodicka, N., 2006. Trans-Hudson orogen of North America and Himalaya-Karakoram-Tibetan orogen of Asia: Structural and thermal characteristics of the lower and upper plates. *Tectonics*, 25 (4), 1–22

St-Onge, M. R., Van Gool, J. A. M., Garde, A. A., Scott, D. J., 2009. Correlation of Archaean and Palaeoproterozoic units between northeastern Canada and western Greenland: constraining the pre-collisional upper plate accretionary history of the Trans-Hudson orogen. *Geological Society, London, Special Publications*, 318 (1), 193–235

Stern, R. J., 2005. Evidence from ophiolites, blueschists, and ultrahigh-pressure metamorphic terranes that the modern episode of subduction tectonics began in Neoproterozoic time. *Geology*, 33 (7), 557–560

Stevenson, D. J., 2003. Styles of mantle convection and their influence on planetary evolution. *Comptes Rendus - Geoscience*, 335 (1), 99–111

Tappe, S., Smart, K. A., Pearson, D. G., Steenfelt, A., Simonetti, A., 2003. Craton formation in Late Archean subduction zones revealed by first Greenland eclogites. *Geology*, 39 (12), 1103–1106

Thompson, D. A., Bastow, I. D., Helffrich, G., Kendall, J. M., Wookey, J., Snyder, D. B., Eaton, D. W., 2010. Precambrian crustal evolution: Seismic constraints from the Canadian Shield. *Earth and Planetary Science Letters*, 297 (3-4), 655–666

Thompson, D. A., Helffrich, G., Bastow, I. D., Kendall, J. M., Wookey, J., Eaton, D. W., Snyder, D. B., 2011. Implications of a simple mantle transition zone beneath cratonic North America. *Earth and Planetary Science Letters*, 312 (1-2), 28–36

Thompson, D. A., Kendall, J.M., Helffrich, G. R., Bastow, I. D., Wookey, J., Snyder, D. B., Snyder, D. B., 2015. CAN-HK: An a Priori Crustal Model for the Canadian Shield. *Seismological Research Letters*, 86 (5), 1374–1382

Tian, Y., Zhao, D., Sun, R., Teng, J., 2009. Seismic imaging of the crust and upper mantle beneath the North China Craton. *Physics of the Earth and Planetary Interiors*, 172 (3-4), 169–182

Vandecar, J. C., Crosson, R.S., 1990. Determination of teleseismic relative phase arrival times using multi-channel cross-correlation and least squares. *Bulletin of the Seismological Society of America*, 80 (1), 150–169

Vandecar, J. C., James, D. E., Assumpcao, M., 1995. Seismic Evidence for a Fossil Mantle Plume beneath South-America and Implications for Plate Driving Forces. *Nature*, 378 (6552), 25–31

Van der Hilst, R., Snieder, R., 1996. High-frequency precursors to P wave arrivals in New Zealand: Implications for slab structure. *Geophysical Journal International: Solid Earth* 101 (B4), 8473–8488

Villemaire, M., Darbyshire, F. A., Bastow, I. D., 2012. P-wave tomography of eastern North America: Evidence for mantle evolution from Archean to Phanerozoic, and modification during subsequent hot spot tectonism. *Journal of Geophysical Research: Solid Earth*, 117, B12302, 15 p

Waldhauser, F., Lippitsch, R., Kissling, E., Ansorge, J., 2002. High-resolution teleseismic tomography of upper-mantle structure using an a priori three-dimensional crustal model. *Geophysical Journal International*, 150 (2), 403–414

Weller, O., St-Onge, M. R., 2017. Record of modern-style plate tectonics in the Palaeoproterozoic Trans-Hudson orogen. *Nature Geoscience*, 10, 305-312

Youssof, M., Thybo, H., Artemieva, I. M., Levander, A., 2015. Upper mantle structure beneath southern African cratons from seismic finite-frequency P- and S-body wave tomography. *Earth and Planetary Science Letters*, 420, 174–186

Yuan, H., Romanowicz, B., 2010. Lithospheric layering in the North American craton. *Nature*, 466, 1063–1068

Yuan, H., Romanowicz, B., Fischer, K. M., Abt, D., 2011. 3-D shear wave radially and azimuthally anisotropic velocity model of the North American upper mantle. *Geophysical Journal International*, 184 (3), 1237–1260

Figure 1. Geological map of Hudson Bay and surrounding areas with Archean material in shades of grey with later eras in color. Boundaries modified from Corrigan et al., (2009). Circles indicate receiver locations. The inset global map shows the location of the receiver network, the red dots are earthquakes used in this study. Yellow dashed line is the approximate extent of the Sugluk block as defined by Berman et al., (2013). SI, Southampton Island; STZ, Snowbird Tectonic Zone; THO, Trans-Hudson Orogen

Figure 2. Example of an unfiltered recording used in this study. Linear and quadratic stacks are the bottom two lines labelled zssl, and zscp, respectively. LEFT: Before application of adaptive stacking method traces are somewhat poorly aligned RIGHT: Clear improvement of alignment as seen from the sharpening of the stacked traces.

Figure 3. (a) Red dots indicate stations that exhibit abrupt residual changes, blue stations are unaffected, grey are inconclusive. (b) Histograms of incidence angle and backazimuth angle anomaly for the abruptly changing residuals, colors match those of the map in (a). (c) Frequency content of rays recorded at all receivers in the network. Comparison between rays from the potential source-side effect (SSE) region and all other rays shows an enhancement of frequency content between 2 and 3 Hz (indicated by the box). (d) Four example stations, three affected, one unaffected.

Figure 4. Earthquakes corresponding to the source-side feature for station FRB plotted against backazimuth and on a map. Residual value is strongly correlated with distance to FRB. Station labels on the map indicate approximate location and distance to the event at the 'peak' of the source-side feature for the three affected stations from Figure 3.

Figure 5. Station map showing network subsets and their respective results of re-stacking for two representative stations. Subsets are indicated by colored loops: Green - Small Model; orange - West Model; pink - East Model. The Large Model group includes all stations in the network.

Figure 6. Tradeoff areas for regularization parameters for S and P wavespeed models. Each colored line represents a single damping value, each dot a different smoothing value. Values for both parameters were varied in the sequence: 0.1, 0.5, 1, 3, 5, 7, 10, 15, 30, 50, 100. The approximate values of the central region are indicated by the green dots and dashed lines.

Figure 7. Checkerboard resolution tests for P and S wave model spaces. Cross-sections A-A* and B-B* shown in the input model are the same for both P and S-wave recovery models. Slices at 180 km depth. Highest resolution is in the central region of the model, the eastern Churchill plate, and the Hudson Strait.

Figure 8. Forward modeling results for stations FRB, LG4Q, and LAIN at backazimuths of 270°-360° through either the top 300 km or bottom 300 km of the full inversion model. These match the stations shown in Figure 3. Tracing through the bottom 300 km model recreates the source-side feature quite well, while tracing through the top 300 km model does not. This indicates that the feature in the backazimuth plots is entirely explained by the deepest structure in the model space, and the upper 300 km seems unaffected. The approximate location of station FRB is indicated by the red text.

Figure 9. The P and S wave inversion depth slices at 150 km depth. Both models reveal broadly similar structure. Variance reduction 75% from $0.11s^2$ for P waves and 78% from $0.8s^2$ for S waves.

Figure 10. Lithospheric cross-sections for both P and S wave inversions along profiles defined in Figure 9. Labels and colors of geological units correspond to Figure 1.

Figure 11. The P and S wave inversion models with cross sections across the Snowbird Tectonic Zone (STZ). Neither model images a velocity distinction across the interface.

Figure 1.

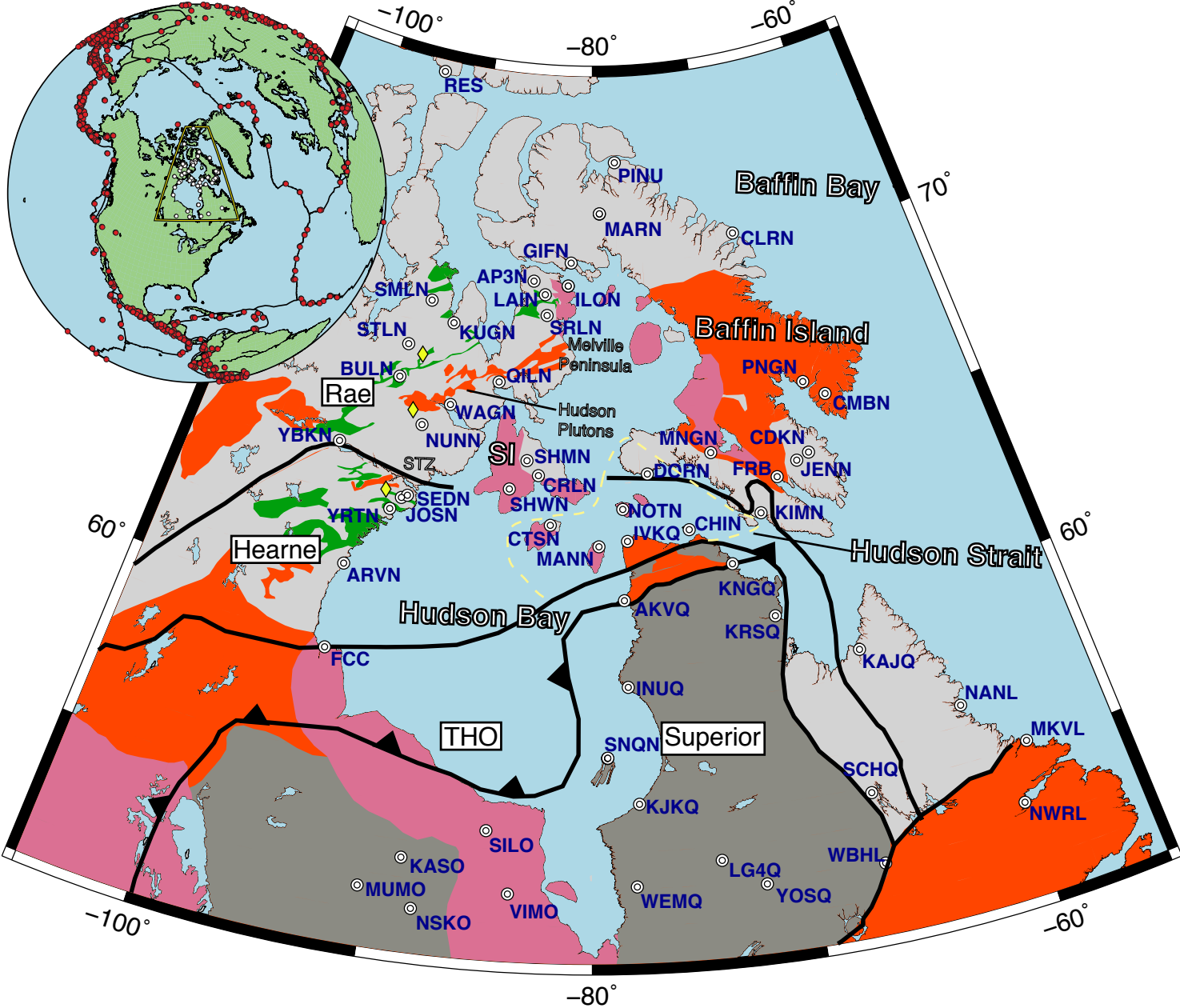
−100°
−80°
−60°
70°
60°
RES
PINU
Baffin Bay
MARN
CLRN
GIFN
AP3N
SMLN
LAIN
ILON
STLN
KUGN
SRLN
Melville
Peninsula
Baffin Island
PNGN
BULN
QILN
CMBN
Rae
WAGN
Hudson
Plutons
YBKN
NUNN
MNGN
CDKN
SI
SHMN
STZ
DCRN
FRB
JENN
CRLN
SEDN
SHWN
NOTN
KIMN
YRTN
JOSN
CHIN
CTSN
IVKQ
Hudson Strait
Hearne
MANN
ARVN
KNGQ
AKVQ
Hudson Bay
KRSQ
FCC
KAJQ
INUQ
NANL
MKVL
THO
SNQN
Superior
SCHQ
KJKQ
NWRL
SILO
WBHL
KASO
LG4Q
MUMO
YOSQ
WEMQ
VIMO
NSKO
−100°
−80°
−60°
60°
ARCHEAN
Churchill
Superior
Greenstone Terranes
Nunavut
Diamond
Prospect
Proterozoic
Sugluk Block
Phanerozoic
Cover

Figure 2.

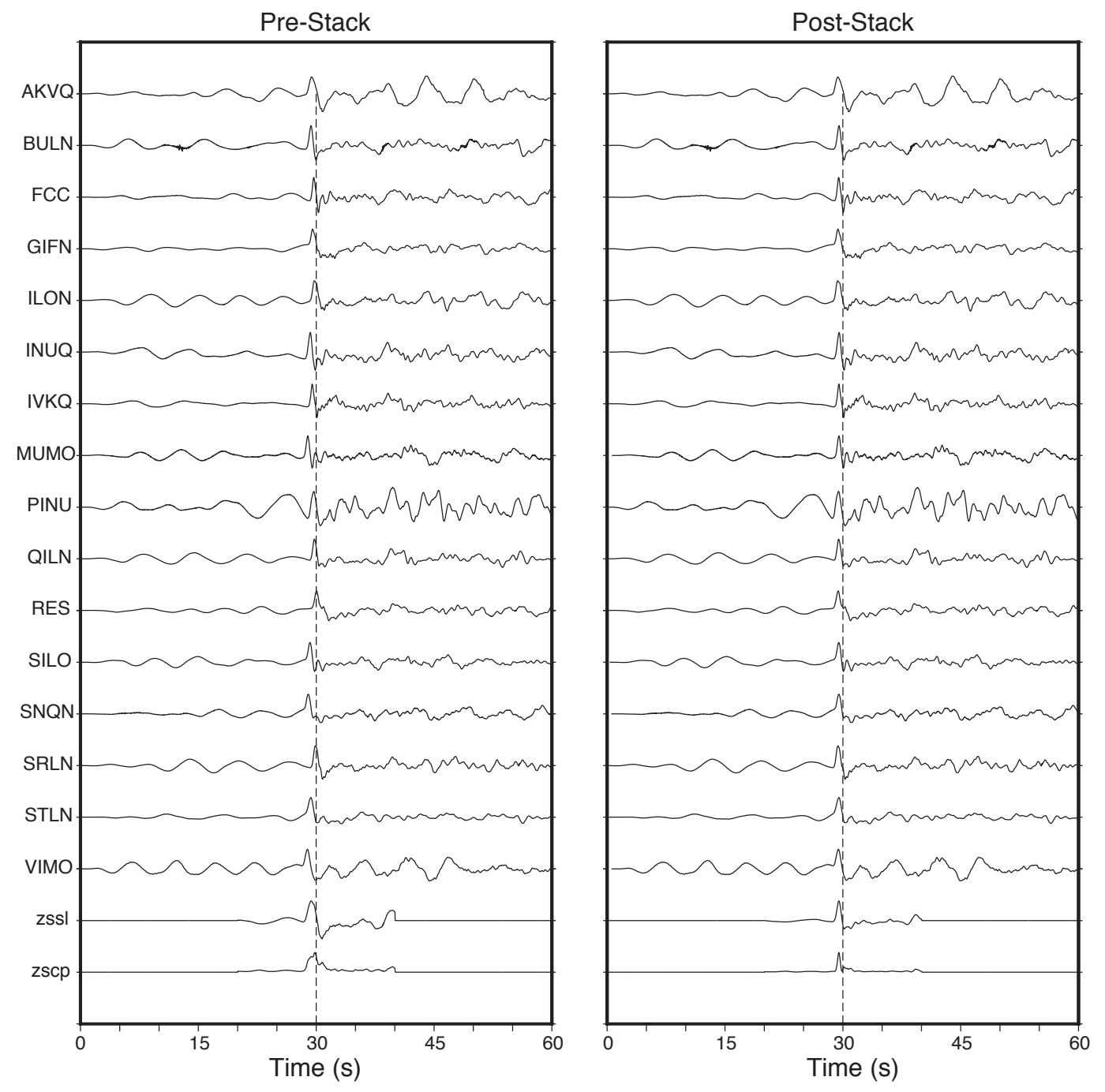
Pre-Stack
Post-Stack
AKVQ
BULN
FCC
GIFN
ILON
INUQ
IVKQ
MUMO
PINU
QILN
RES
SILO
SNQN
SRLN
STLN
VIMO
zssl
zscp
0
15
30
45
60
Time (s)
0
15
30
45
60
Time (s)

Figure 3.

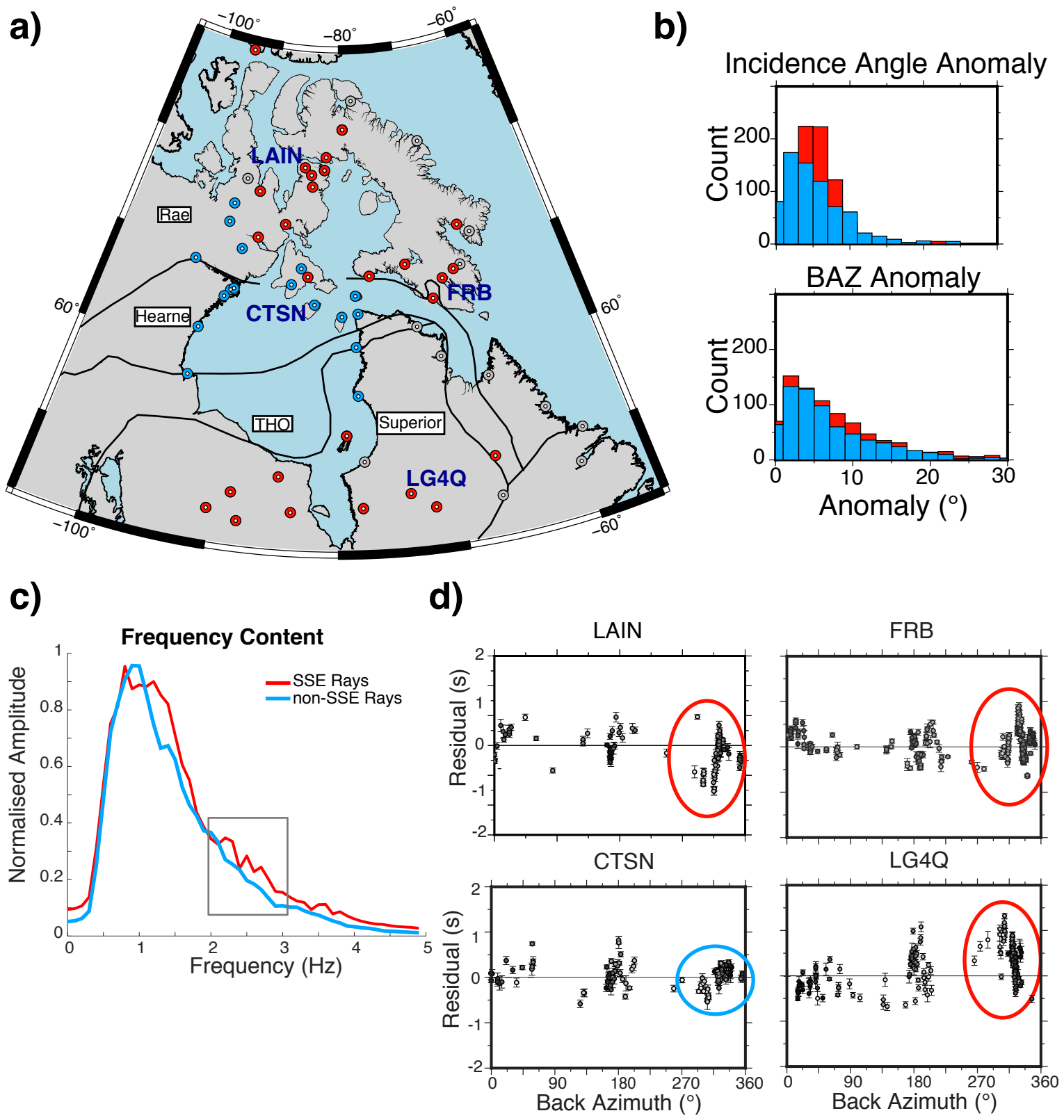
a)
−100°
−80°
−60°
60°
60°
−100°
−60°
LAIN
Rae
FRB
Hearne
CTSN
THO
Superior
LG4Q
b)
Incidence Angle Anomaly
Count
200
100
0
BAZ Anomaly
Count
200
100
0
0
10
20
30
Anomaly (°)
c)
Frequency Content
SSE Rays
non-SSE Rays
Normalised Amplitude
1
0.8
0.6
0.4
0.2
0
0
1
2
3
4
5
Frequency (Hz)
d)
LAIN
FRB
CTSN
LG4Q
Residual (s)
2
1
0
-1
-2
0
90
180
270
360
Back Azimuth (°)

Figure 4.

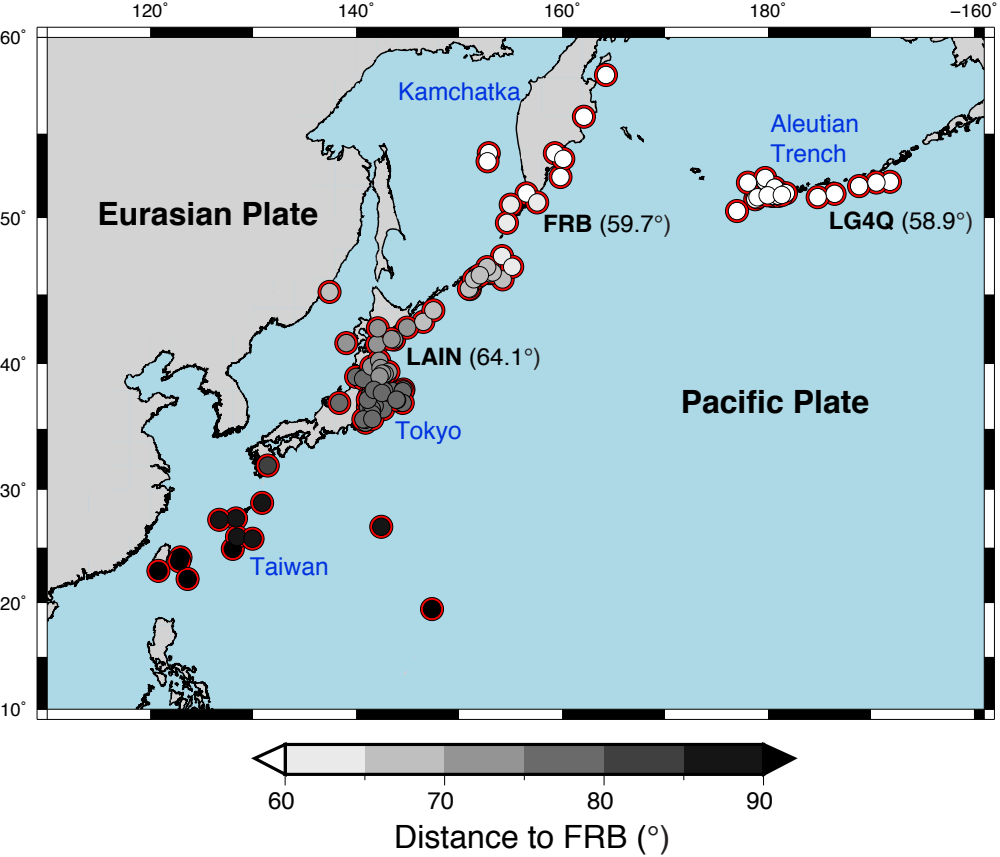
120°
140°
160°
180°
−160°
60°
50°
40°
30°
20°
10°
Kamchatka
Aleutian
Trench
Eurasian Plate
FRB (59.7°)
LG4Q (58.9°)
LAIN (64.1°)
Pacific Plate
Tokyo
Taiwan
60
70
80
90
Distance to FRB (°)

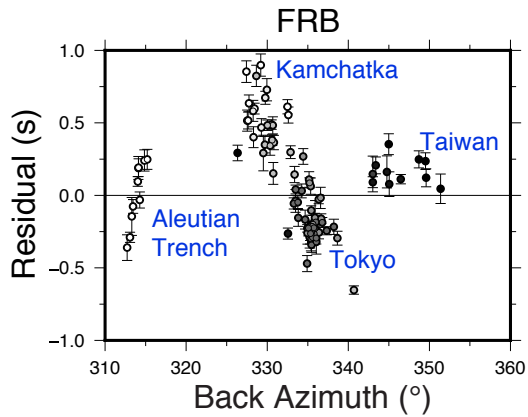
FRB
Residual (s)
1.0
0.5
0.0
−0.5
−1.0
Kamchatka
Taiwan
Aleutian
Trench
Tokyo
310
320
330
340
350
360
Back Azimuth (°)

Figure 5.

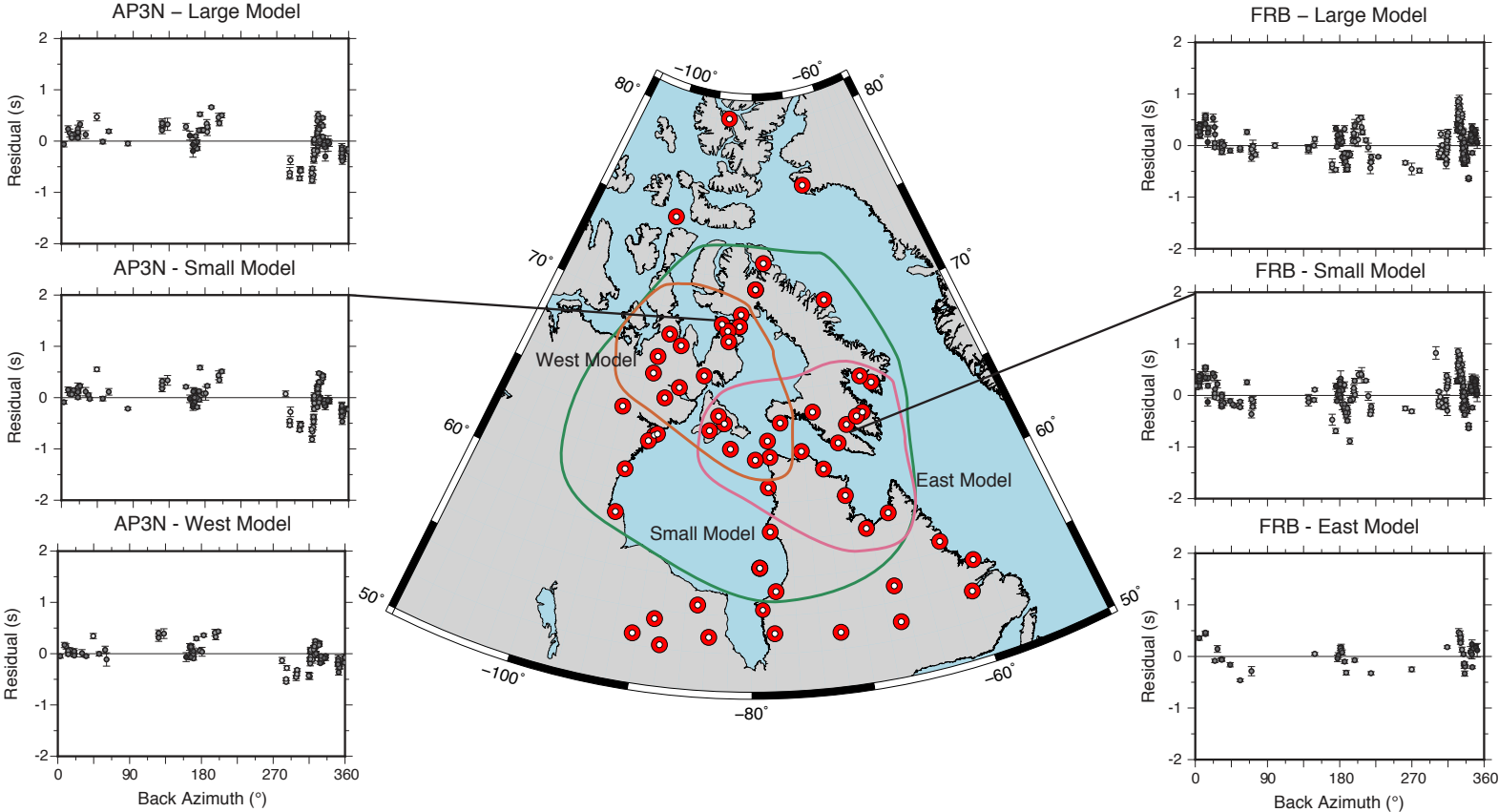
AP3N – Large Model
AP3N - Small Model
AP3N - West Model
FRB – Large Model
FRB - Small Model
FRB - East Model
Residual (s)
Back Azimuth (°)
West Model
East Model
Small Model
80°
70°
60°
50°
−100°
−60°
−80°

Figure 6.

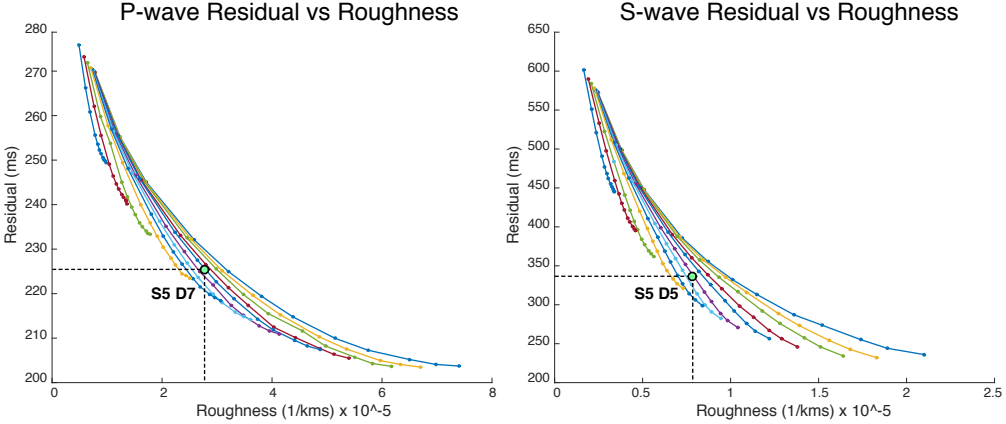
P-wave Residual vs Roughness
Residual (ms)
Roughness (1/kms) x 10^-5
S5 D7
S-wave Residual vs Roughness
Residual (ms)
Roughness (1/kms) x 10^-5
S5 D5

Figure 7.

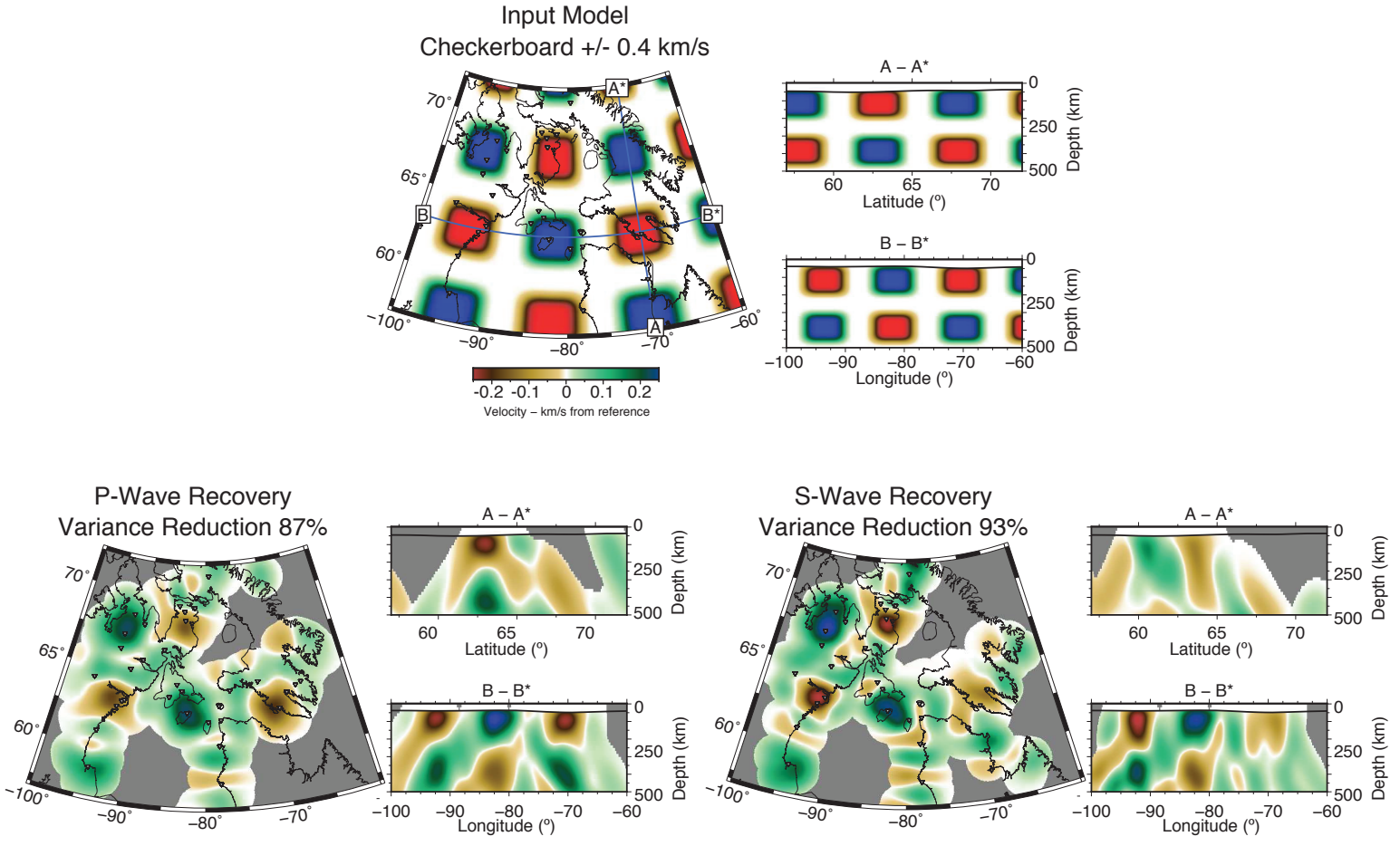
Input Model
Checkerboard +/- 0.4 km/s
A*
B
B*
A
70°
65°
60°
−100°
−90°
−80°
−70°
−60°
-0.2 -0.1 0 0.1 0.2
Velocity – km/s from reference
A – A*
B – B*
Depth (km)
0
250
500
60
65
70
Latitude (°)
−100
−90
−80
−70
−60
Longitude (°)
P-Wave Recovery
Variance Reduction 87%
S-Wave Recovery
Variance Reduction 93%

Figure 8.

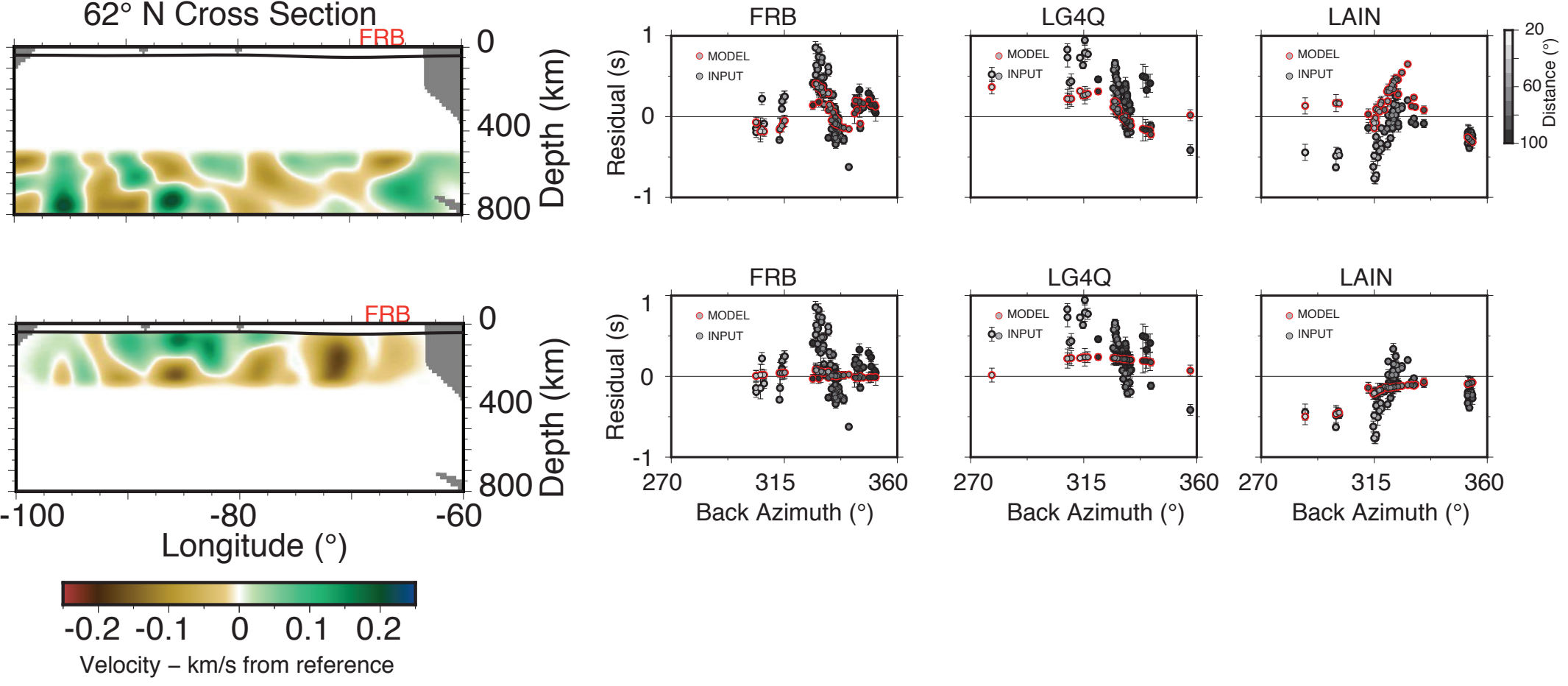
62° N Cross Section
FRB
0
400
800
Depth (km)
FRB
0
400
800
Depth (km)
-100
-80
-60
Longitude (°)
-0.2 -0.1 0 0.1 0.2
Velocity – km/s from reference
FRB
LG4Q
LAIN
MODEL
INPUT
Residual (s)
1
0
-1
270
315
360
Back Azimuth (°)
20
60
100
Distance (°)

Figure 9.

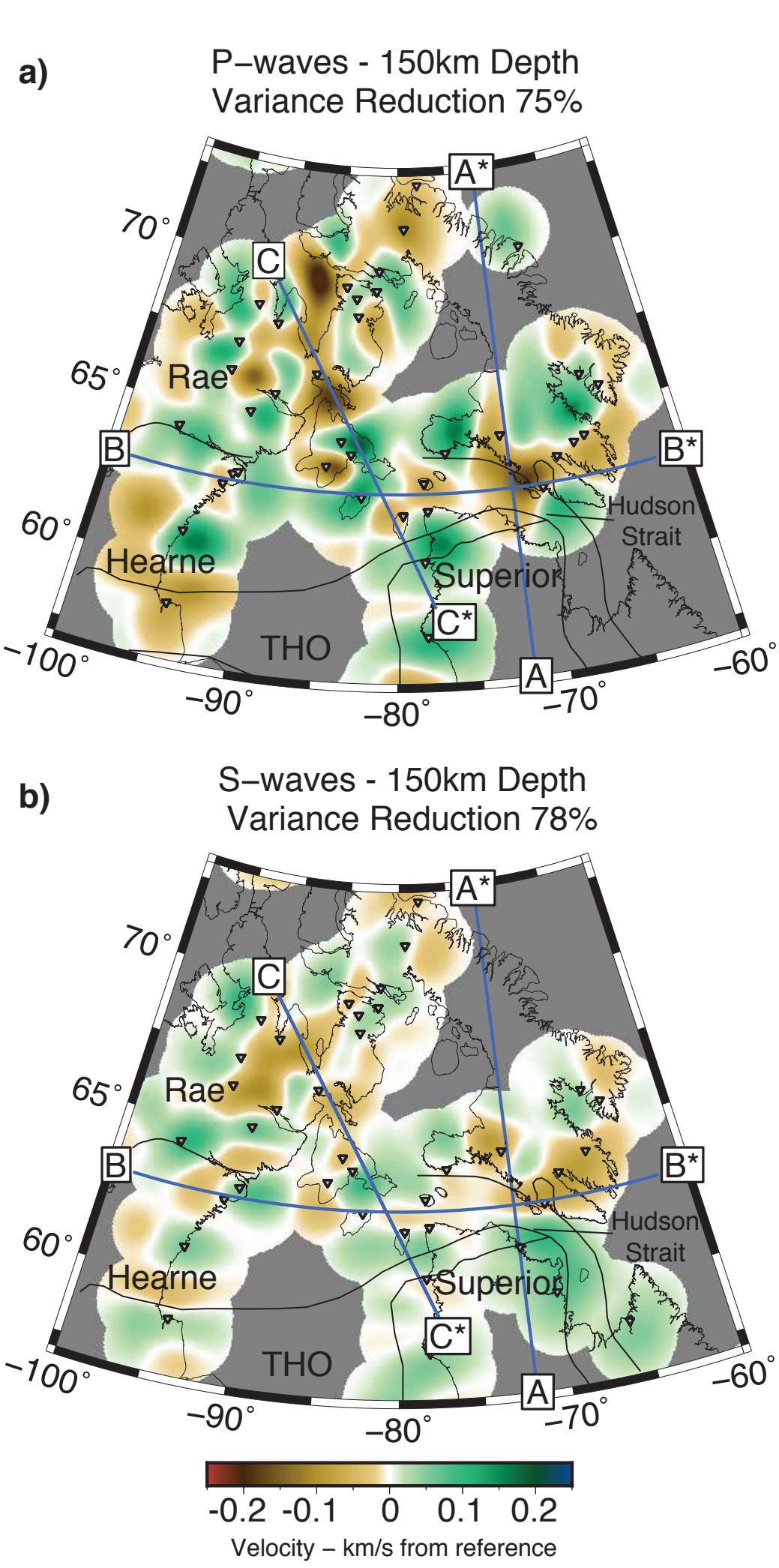
a)
P–waves - 150km Depth
Variance Reduction 75%
A*
C
70°
65°
Rae
B
B*
60°
Hudson
Strait
Hearne
Superior
C*
THO
A
–100°
–90°
–80°
–70°
–60°
b)
S–waves - 150km Depth
Variance Reduction 78%
A*
C
70°
65°
Rae
B
B*
60°
Hudson
Strait
Hearne
Superior
C*
THO
A
–100°
–90°
–80°
–70°
–60°
-0.2 -0.1 0 0.1 0.2
Velocity – km/s from reference

Figure 10.

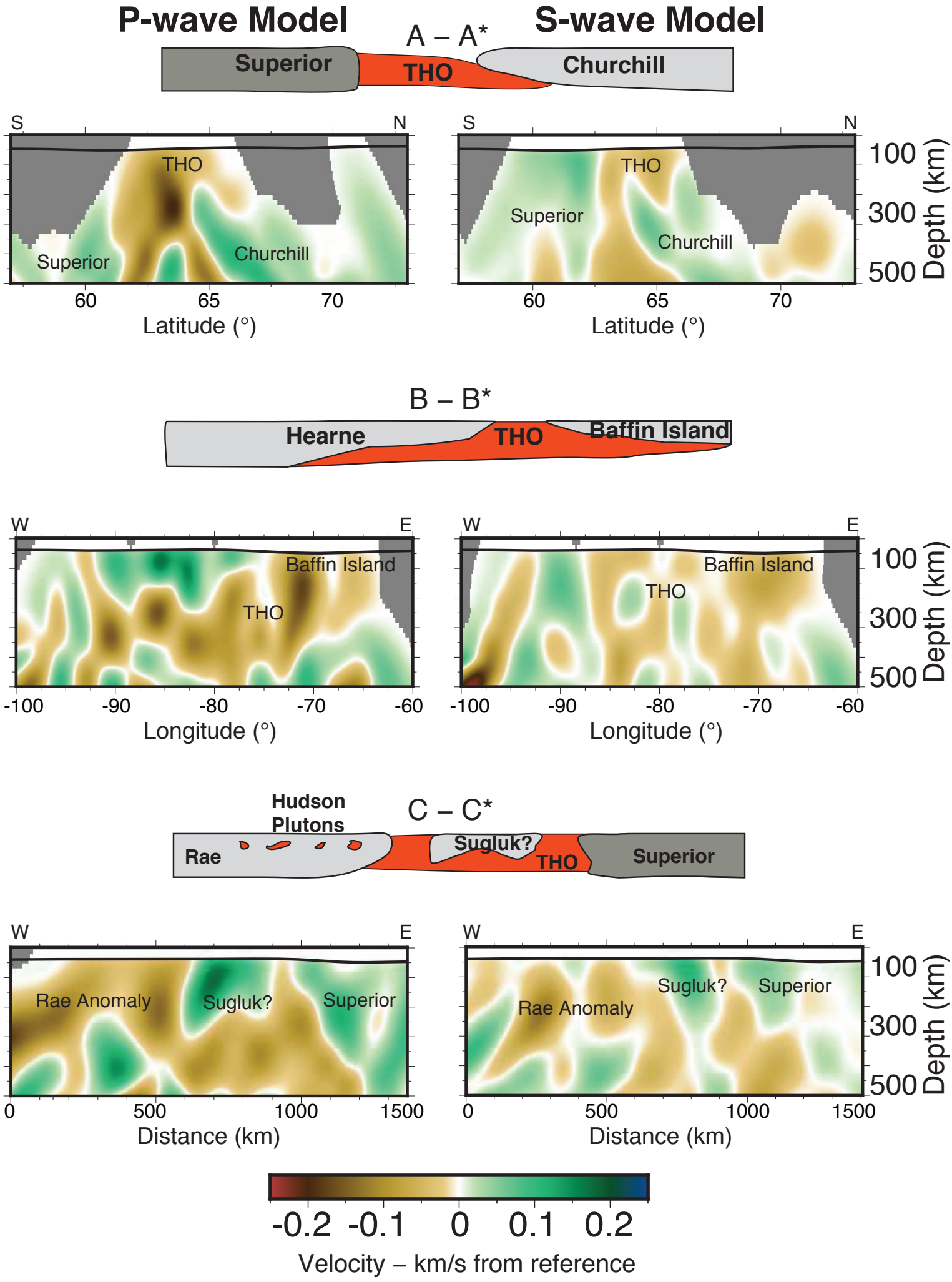
P-wave Model
S-wave Model
A – A*
Superior
THO
Churchill
S
N
THO
Superior
Churchill
60
65
70
Latitude (°)
100
300
500
Depth (km)
B – B*
Hearne
THO
Baffin Island
W
E
Baffin Island
THO
-100
-90
-80
-70
-60
Longitude (°)
C – C*
Hudson
Plutons
Rae
Sugluk?
THO
Superior
Rae Anomaly
Sugluk?
Superior
0
500
1000
1500
Distance (km)
-0.2
-0.1
0
0.1
0.2
Velocity – km/s from reference

Figure 11.

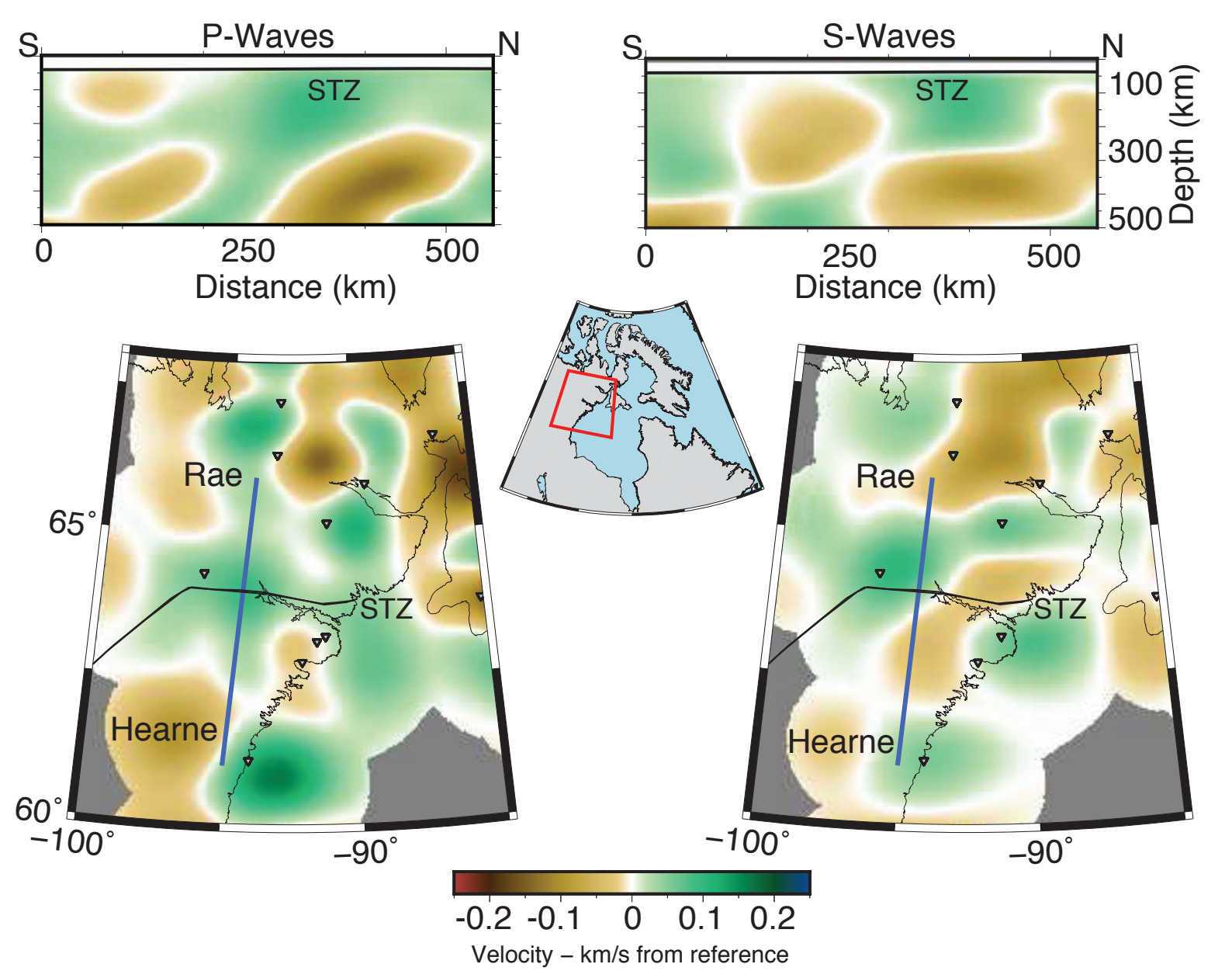
P-Waves
S
N
STZ
0
250
500
Distance (km)
S-Waves
S
N
STZ
100
300
500
Depth (km)
0
250
500
Distance (km)
Rae
Hearne
STZ
65°
60°
−100°
−90°
Rae
Hearne
STZ
−100°
−90°
-0.2 -0.1 0 0.1 0.2
Velocity – km/s from reference